This is Volume 36 in
INTERNATIONAL GEOPHYSICS SERIES

A Series of Monographs and Textbooks

Edited by WILLIAM L. DONN

The complete listing of books in this series is available from the publisher.

THEORY OF PLANETARY ATMOSPHERES

An Introduction to Their Physics and Chemistry

Second Edition

Joseph W. Chamberlain

Department of Space Physics and Astronomy
Wiess School of Natural Sciences
Rice University
Houston, Texas

In collaboration with

Donald M. Hunten

Department of Planetary Sciences
Lunar and Planetary Laboratory
University of Arizona
Tucson, Arizona

ACADEMIC PRESS, INC.
Harcourt Brace Jovanovich, Publishers
San Diego New York Berkeley Boston
London Sydney Tokyo Toronto

Several of my colleagues have read chapters of the text in draft and made constructive suggestions. I am especially indebted to Donald E. Anderson, Ralph J. Cicerone, Von R. Eshleman, Donald M. Hunten, Andrew A. Lacis, and Darrell R. Strobel for very critical and helpful readings. The text and the drawings have been prepared by Christine Dunning; I am most grateful to her for the high quality of her work and for a constant good humor, both of which lightened my burdens enormously.

Chapter 1
VERTICAL STRUCTURE OF AN ATMOSPHERE

The simplest conceivable atmosphere is gravitationally bound (and therefore in hydrostatic equilibrium) and spherically symmetric. For the terrestrial planets, at least, solar radiation and the radiative properties of the atmospheric constituents fix the first-order description of the vertical thermal structure. An atmosphere controlled by sunlight can scarcely be spherically symmetric. Nevertheless, it is useful to think of a mean planetary atmosphere, with day–night and latitudinal variations occurring about the mean.

The *vertical structure* of an atmosphere is the run of pressure, temperature, density, and chemical composition with distance from the center of the planet (or with height above the surface). When these parameters are inferred in part from theory or when they are tabulated as mean or representative values, they constitute a *model atmosphere.*

Figure 1.1 shows the temperature profile for Earth's atmosphere; it serves to divide the atmosphere into different regions, where the controlling physics and chemistry differ.

The tropospheric temperature is governed by radiative and convective exchange. In the stratosphere trace amounts of O_3 are formed by sunlight; the remarkable ability of O_3 to absorb both ultraviolet and infrared radiation causes an inversion above the tropopause. The decrease in O_3 production and the increased rate of cooling to space by CO_2 reestablish a declining

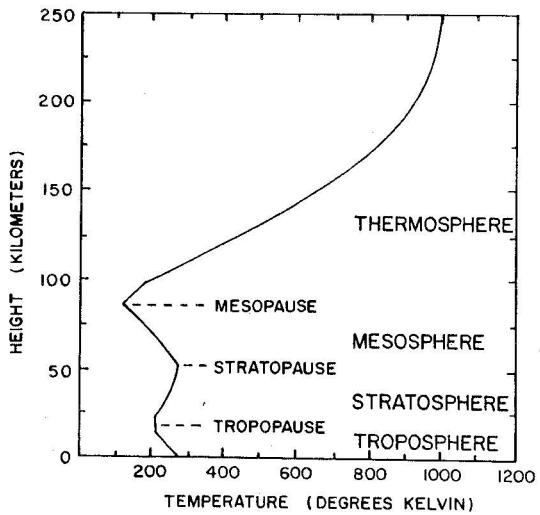

Fig. 1.1 Schematic temperature profile for Earth's atmosphere showing the various regimes defined by the temperature gradient.

temperature in the mesosphere. Finally, heating by O_2 photolysis and ionization increases the thermosphere temperatures to about 1000°K. We shall examine the main processes in these regions in turn.

1.1 Hydrostatic Equilibrium

The vertical distribution of pressure, temperature, and density in a static, spherical atmosphere with a specified composition are governed by three relationships. First we have hydrostatic equilibrium, in which the pressure gradient is

$$\frac{dp}{dr} = -\left(\frac{G\mathcal{M}}{r^2}\right)(MN) = -g(r)\rho \tag{1.1.1}$$

Here $\mathcal{M}$ is the mass of the planet and M is the mean mass of the molecules of a mixed atmosphere, N is their number density, ρ is the mass density, and r is the distance from the center of the (spherical) planet. Over height intervals Δr such that $\Delta r \ll r$, the local acceleration of gravity $g(r) \approx$ const.

For an equation of state, the perfect gas law is adequate:

$$p = NkT = \rho RT \tag{1.1.2}$$

where $R = k/M$ (erg/gm deg) is the gas constant appropriate to the atmospheric composition. Then hydrostatic equilibrium gives

$$\frac{dp}{p} = -\frac{G\mathcal{M}M}{kT}\frac{dr}{r^2} \approx -\frac{gM}{kT}\,dz \equiv -\frac{dz}{H} \tag{1.1.3}$$

where z is height above the surface and H the (pressure) *scale height*.

A third relation must fix the temperature (cf. Section 1.2). If the mean mass and temperature are constant with height, we obtain the *barometric law*:

$$\begin{aligned} p(r) &= p(r_0)\exp\left(-\frac{G\mathcal{M}M}{kTrr_0}(r - r_0)\right) \\ &\approx p(r_0)\exp\left(-\frac{r - r_0}{H}\right) \\ p(z) &= p(z_0)\exp\left(-\frac{z - z_0}{H}\right) \end{aligned} \tag{1.1.4}$$

Thus the *pressure scale height* ($H = kT/Mg$) is an e-folding distance. In the general case the density distribution is

$$\begin{aligned} \frac{dN}{N} &= -\frac{dT}{T} - \frac{G\mathcal{M}M}{kT}\frac{dr}{r^2} \approx -\frac{dT}{T} - \frac{dz}{H} \\ &= -\left(\frac{1}{T}\frac{dT}{dz} + \frac{Mg}{kT}\right)dz = -\frac{dz}{H^*} \end{aligned} \tag{1.1.5}$$

which defines the *density scale height* H^*. The *integrated density* is the number of particles in a column above a specified height. It is, from (1.1.1),

$$\begin{aligned} \mathcal{N}(r) &\equiv \int_r^\infty N(r)\,dr = \int_0^{p(r)} \frac{r^2}{G\mathcal{M}M}\,dp \\ &\approx \frac{p(r)}{g(r)M} = N(r)H \end{aligned} \tag{1.1.6}$$

The integrated density is often written in terms of the height of a column under standard temperature and pressure conditions that would contain the same number of molecules or atoms. This is the equivalent thickness in "atmo-centimeters" (alternatively, "centimeter-atmospheres" or "centimeter-amagat"),

$$\xi = \frac{\mathcal{N}(z)}{N_0}\ \text{atm-cm} \tag{1.1.7}$$

where N_0 is Loschmidt's number (2.687×10^{19} cm^{-3}).

Without perfect mixing the mean mass M is a function of height, $M(z)$. At high altitudes the mixing processes are likely to be less important since the diffusion coefficient (Section 2.3.1) is large. Hence the atmosphere tends to separate out diffusively, and the composition changes as well through photochemical reactions. The gravity g is also a function of height [see (1.1.3)]. This effect is discussed in Section 7.1; the generalized barometric equation is (7.1.19).

1.2 Radiative Equilibrium

As a starting point we will regard the atmospheric temperature as governed by radiative equilibrium. Of course, it is not, but we will add convection later. In the ionosphere conduction becomes the dominant mechanism for heat transfer, and radiative equilibrium is not even a good starting approximation.

1.2.1 Equation of Radiative Transfer and Kirchhoff's Law

In a homogeneous medium (see Fig. 1.2) the monochromatic radiant intensity I_ν (measured in erg/cm^2 sec sr Hz) changes along distance ds (measured in the direction of propagation of the light ray and always positive) by amount dI_ν given by

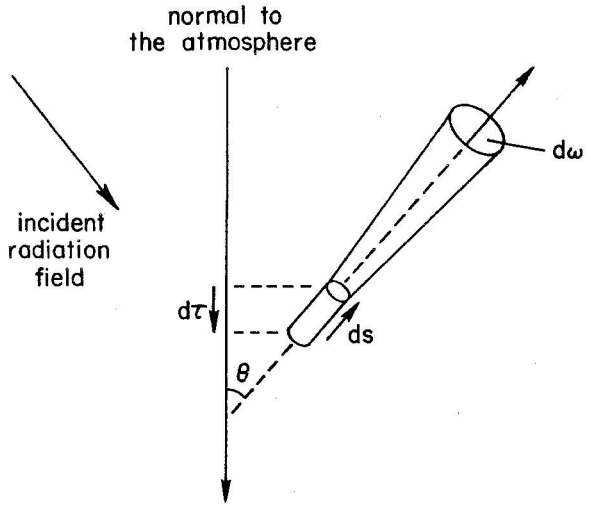

Fig. 1.2 Geometry for the equation of radiative transfer. The element ds is always positive and taken in the direction of propagation of a light ray.

$$\frac{1}{\rho}\frac{dI_\nu}{ds} = -(\kappa_\nu + \sigma_\nu)I_\nu + j_\nu \tag{1.2.1}$$

where κ_ν is the mass absorption coefficient and σ_ν the mass scattering coefficient (both measured in cm^2/gm), and j_ν is the emission coefficient (erg/gm sec sr Hz). The emission j_ν may be due in part to scattering and in part to thermal excitation. The combination $\kappa_\nu + \sigma_\nu$ is the *extinction coefficient.*

Let us look at a few special cases. If emission and scattering back into the original beam are negligible, as in viewing a single star against a black sky, we have $j_\nu = 0$ and

$$I_\nu(s) = I_\nu(0)e^{-(\kappa_\nu+\sigma_\nu)\rho s} \tag{1.2.2}$$

which is *Lambert's exponential absorption law.*

If the source of emission includes scattering (as in the blue, sunlit sky), we have to specify a *scattering phase function*, $p(\cos\Theta)$, giving the angular distribution of scattered radiation. Thus, if j_ν is entirely due to scattering, the emission term is

$$j_\nu = \frac{\kappa_\nu + \sigma_\nu}{4\pi}\int I_\nu(\cos\Theta)p(\cos\Theta)\,d\Omega' \tag{1.2.3}$$

where the phase function itself is normalized so that integrated over a sphere it is

$$\frac{1}{4\pi}\int p(\cos\Theta)\,d\Omega' = \frac{\sigma_\nu}{\kappa_\nu + \sigma_\nu} \equiv \tilde{\omega}_\nu \tag{1.2.4}$$

which is called the *albedo for single scattering.*

For the scattering atmosphere, then, the equation of transfer is, for radiation in direction θ, ϕ,

$$\frac{dI_\nu(\theta,\phi)}{(\kappa_\nu+\sigma_\nu)\rho\,ds} = -I_\nu(\theta,\phi) + \frac{1}{4\pi}\int_0^{2\pi}\int_0^{\pi} I_\nu(\theta',\phi')p(\theta,\phi;\theta',\phi')\sin\theta'\,d\theta'\,d\phi' \tag{1.2.5}$$

At the other extreme from a scattering atmosphere is one in *local thermodynamic equilibrium* (LTE). It is assumed that at each point a local temperature T can be defined so that the emission is given by Kirchhoff's law,

$$j_\nu = \kappa_\nu B_\nu(T) \tag{1.2.6}$$

where the Planck function is

$$B_\nu(T) = \frac{2h\nu^3}{c^2}\frac{1}{e^{h\nu/kT}-1} \tag{1.2.7}$$

We then have, since σ_ν is assumed zero, the monochromatic radiation in LTE given by

$$\frac{dI_\nu(\theta,\phi)}{\kappa_\nu \rho\, ds} = -I_\nu(\theta,\phi) + B_\nu(T) \tag{1.2.8}$$

The LTE approximation can never be exact, and one problem is ascertaining how inexact it is. In complete thermodynamic equilibrium, the temperature is everywhere the same; in the atmosphere the temperature has a definite gradient. Also, atmospheric emission is not Planckian at any point; the radiation field in the ultraviolet and infrared are not characteristic of the same T. Finally, the local kinetic temperature (given by the Maxwellian distribution law) is not the same as the effective Planckian temperature (defined by the radiation field). In a real situation we must usually treat scattering and thermal emission together. For combined isotropic scattering and thermal emission the transfer equation is

$$\frac{dI_\nu}{(\kappa_\nu+\sigma_\nu)\rho\, ds} = -I_\nu + \frac{\tilde{\omega}_\nu}{4\pi}\int_0^{2\pi}\int_{-\pi/2}^{\pi/2} I_\nu(\theta',\phi')\sin\theta'\, d\theta'\, d\phi' + (1-\tilde{\omega}_\nu)B_\nu \tag{1.2.9}$$

In the general case we define the source function (in the same units as I_ν) as the ratio of emission coefficient to opacity

$$\mathcal{J}_\nu = \frac{j_\nu}{\kappa_\nu+\sigma_\nu} \tag{1.2.10}$$

Then the general equation of transfer is

$$\frac{dI_\nu}{(\kappa_\nu+\sigma_\nu)\rho\, ds} = -I_\nu + \mathcal{J}_\nu \tag{1.2.11}$$

For isotropic scattering,

$$\mathcal{J}_\nu = \frac{\tilde{\omega}_\nu}{4\pi}\int I_\nu\, d\Omega \equiv \tilde{\omega}_\nu J_\nu \tag{1.2.12}$$

where J_ν is the local mean intensity. For LTE,

$$\mathcal{J}_\nu = B_\nu(T) \tag{1.2.13}$$

and the combined case has

$$\mathcal{J}_\nu = \tilde{\omega}_\nu J_\nu + (1-\tilde{\omega}_\nu)B_\nu \tag{1.2.14}$$

Defining a *slant optical thickness* from s to s' as

$$\tau_\nu(s,s') = \int_s^{s'} (\kappa_\nu+\sigma_\nu)\rho\, ds \tag{1.2.15}$$

we can write down the formal solution to Eq. (1.2.11) as

$$I_\nu(s) = I_\nu(0)e^{-\tau_\nu(s,0)} + \int_0^s \mathcal{J}_\nu(s')e^{-\tau_\nu(s,s')}(\kappa_\nu+\sigma_\nu)\rho\, ds' \tag{1.2.16}$$

If the source function is known, we have the solution for the radiation field. In practice, the solution is not so simple because $\mathcal{J}_\nu(s')$ depends on $I_\nu(s')$ directly or on $B_\nu(T)$ (which in turn depends on the heating from the radiation field) or both.

1.2.2 Monochromatic Radiative Equilibrium

In a plane-stratified atmosphere in which height z is measured upward, we measure optical depth τ downward and zenith angle of the direction of radiation flow θ from the upward vertical. Then $ds = \sec\theta\, dz$ is always positive and the vertical optical thickness is

$$d\tau_\nu = -(\kappa_\nu+\sigma_\nu)\rho\, dz \tag{1.2.17}$$

Equation (1.2.8) for LTE conditions is then

$$\mu\frac{dI_\nu(\theta,\phi)}{d\tau_\nu} = I_\nu(\theta,\phi) - B_\nu(T) \tag{1.2.18}$$

where $\mu = \cos\theta$. Integrating over a sphere we have

$$\frac{d}{d\tau_\nu}(\pi F_\nu) = 4\pi(J_\nu - B_\nu) \tag{1.2.19}$$

where the mean intensity J_ν is given by (1.2.12) and the net flux across an area parallel to the surface is

$$\pi F_\nu = 2\pi\int_{-1}^{1} I_\nu(\mu)\mu\, d\mu \tag{1.2.20}$$

We may obtain an approximate solution by the *two-stream approximation* (see Fig. 1.3). Suppose that the upward radiant intensity is $I_\nu(\mu,\tau) = I^+(\tau)$

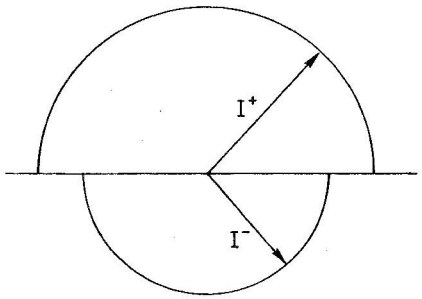

Fig. 1.3 The two-stream approximation considers the radiation field to be composed of two simple streams, one upward and one downward.

for $0 < \mu < +1$ and the downward radiation field is $I_\nu(\mu, \tau) = I^-(\tau)$ $(-1 < \mu < 0)$. Then the mean intensity at depth τ is

$$J_\nu \equiv \tfrac{1}{2}\int_{-1}^{1} I_\nu(\mu)\, d\mu = \tfrac{1}{2}(I^+ + I^-) \tag{1.2.21}$$

and the net flux is

$$\pi F_\nu = \pi(I^+ - I^-) \tag{1.2.22}$$

To obtain a second relation between mean intensity and flux, we multiply (1.2.18) by μ and integrate over a sphere. With (1.2.20) and (1.2.21) we have

$$2\pi \frac{d}{d\tau_\nu}\int_0^1 d\mu\, \mu^2(I^+ + I^-) = 2\pi \int_0^1 d\mu\, \mu(I^+ - I^-) \tag{1.2.23}$$

or

$$\frac{4\pi}{3}\frac{dJ_\nu}{d\tau_\nu} = \pi F_\nu \tag{1.2.24}$$

Substituting (1.2.19) for J_ν in this equation yields the flux equation

$$\frac{d^2 F_\nu}{d\tau_\nu^2} - 3F_\nu = -4\frac{dB_\nu}{d\tau_\nu} \tag{1.2.25}$$

The concept of radiative equilibrium means that the net flux divergence is everywhere zero, with no energy lost or supplied by convection or conduction. It does not mean that the flux πF_ν in each separate frequency everywhere is constant. Nevertheless, it is instructive to examine this case of *monochromatic radiative equilibrium* (MRE). With $dF_\nu/d\tau_\nu = 0$ everywhere, our equation for the thermal radiation versus τ_ν is

$$\frac{dB_\nu}{d\tau_\nu} = \tfrac{3}{4}F_\nu = \text{const} \tag{1.2.26}$$

In applying boundary conditions we have to be careful that they do not conflict with assumptions already introduced in the two-stream approximation. Let us suppose that the ground is a black body at temperature T_g and a cold black sky ($T = 0$) lies above the atmosphere. With Eqs. (1.2.21) and (1.2.22) we can write

$$J_\nu = I^- + \tfrac{1}{2}F_\nu = I^+ - \tfrac{1}{2}F_\nu \tag{1.2.27}$$

Then the transfer equation (1.2.19) gives

$$\begin{aligned}\frac{dF_\nu}{d\tau_\nu} &= 4(I^+ - B_\nu) - 2F_\nu \\ &= 4(I^- - B_\nu) + 2F_\nu = 0\end{aligned} \tag{1.2.28}$$

Hence the upward intensity at the ground is

$$I_g{}^+ \equiv B_\nu(T_g) = B_\nu(T_1) + \tfrac{1}{2}F_\nu \tag{1.2.29}$$

where T_1 is the air temperature at the ground, and the downward intensity at the top of the atmosphere is

$$I_0{}^- \equiv 0 = B_\nu(T_0) - \tfrac{1}{2}F_\nu \tag{1.2.30}$$

where T_0 is the air temperature at $\tau = 0$.

The solution tells us that, to fit an LTE solution with the special case of MRE, there is a discontinuity in temperature at the ground, with $T_g > T_1$, and the air at the top approaches a value, $T_0 \neq 0$. The radiant flux leaving the atmosphere is

$$\pi I_0{}^+ = \pi B_\nu(T_0) + \frac{\pi}{2}F_\nu = 2\pi B_\nu(T_0) \tag{1.2.31}$$

or twice what an opaque black body at temperature T_0 would emit.

The solution, then, from (1.2.26) and (1.2.30) is (see Fig. 1.4)

$$B_\nu(\tau_\nu) = B_\nu(T_0)(1 + \tfrac{3}{2}\tau_\nu) \tag{1.2.32}$$

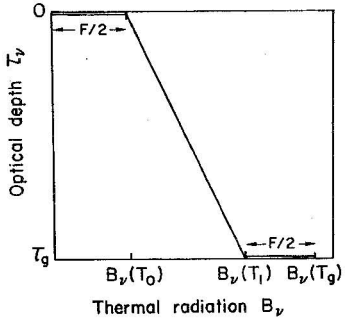

Fig. 1.4 The MRE solution for $T(\tau)$, presented as $B_\nu(T)$ vs. τ_ν. Note the discontinuity at the ground and the finite skin temperature at $\tau = 0$.

The atmospheric radiation πI_0^+ is thus characteristic of the thermal emission at $\tau_\nu = \frac{2}{3}$.

A common name for T_0 is the *Gold–Humphreys skin temperature*, or simply *skin temperature*. It can be derived on the assumption that a volume element in the stratosphere is heated by absorption of planetary radiation over a hemisphere and cooled by its own radiation over a sphere. By Kirchhoff's law, the absorption and emission are proportional as long as the same wavelength bands are involved, which is approximately true. Since the solid angles are in a ratio 1:2, the mean planetary temperature and the skin temperature are in the ratio $1:2^{-1/4}$ [cf. (1.2.45)]. The principal reason for deviations from this result is additional heating by solar radiation; a prominent example is ozone heating on the Earth.

1.2.3 Local Thermodynamic Equilibrium for a Gray Atmosphere Heated from the Ground

We are now ready to examine how the interchange of radiation governs the temperature of an atmosphere when there is no direct solar absorption by the atmosphere, when there is no conduction or convection, and when scattering can be neglected. The transfer equation (1.2.8) for LTE is

$$\frac{\mu\, dI_\nu}{\kappa_\nu \rho\, dz} = -I_\nu + B_\nu \tag{1.2.33}$$

Integrating over frequency we have

$$\frac{\mu}{\rho}\frac{d}{dz}\left(\int_0^\infty \frac{I_\nu}{\kappa_\nu}\, d\nu\right) = -I + B \tag{1.2.34}$$

where

$$I = \int_0^\infty I_\nu\, d\nu, \qquad B = \int_0^\infty B_\nu\, d\nu \tag{1.2.35}$$

By integrating over a sphere and setting the net flux constant, we have, analogously to Eq. (1.2.26),

$$-\frac{1}{\rho}\frac{d}{dz}\left(\int_0^\infty \frac{B_\nu}{\kappa_\nu}\, d\nu\right) = \tfrac{3}{4}F \tag{1.2.36}$$

where $F = \int F_\nu\, d\nu$. In the event $\kappa_\nu = \text{const}\ (=\kappa)$ the transfer equation (1.2.33) is

$$\mu\frac{dI}{d\tau} = I - B \tag{1.2.37}$$

and the thermal radiation is given by

$$\frac{dB}{d\tau} = \tfrac{3}{4}F \tag{1.2.38}$$

where

$$d\tau = -\kappa\rho\, dz \tag{1.2.39}$$

Hence the gray solution is analogous to that for MRE given above.

It would seem that, with a mean absorption coefficient properly defined, any nongray atmosphere could be treated with the gray solution. Thus writing

$$d\tau = -\langle\kappa\rangle\rho\, dz \tag{1.2.40}$$

a comparison of (1.2.36) and (1.2.38) suggests

$$\frac{1}{\langle\kappa\rangle} = \frac{1}{B}\int_0^\infty \frac{B_\nu}{\kappa_\nu}\, d\nu \tag{1.2.41}$$

where B is given by (1.2.35). This $\langle\kappa\rangle$ is the *Rosseland mean* used widely in astrophysics. The problem with it lies in the Eddington approximation. To conserve flux, the MRE equation (1.2.19) requires $J_\nu = B_\nu$ precisely. But in LTE there is a gradual shift with depth in the frequency distribution of the radiation, since temperature varies with depth, and J_ν cannot precisely equal B_ν to conserve the flux in each frequency interval. But if there is approximate equality over the spectrum, the Rosseland mean is a good approximation. It works well for stellar atmospheres, but is not good for most terrestrial situations. Since T and $B_\nu(T)$ vary with depth, $\langle\kappa\rangle$ cannot be treated as constant with depth. Thus iterations are required to compute $B_\nu(T)$ and $\langle\kappa\rangle$ as functions of depth. An alternative and generally better procedure is to put κ_ν on the right-hand side of (1.2.26) and integrate over ν. Comparison with (1.2.38) gives

$$\langle\kappa\rangle = \frac{1}{F}\int_0^\infty \kappa_\nu F_\nu\, d\nu \tag{1.2.42}$$

which is the *Chandrasekhar mean* coefficient. Its difficulty is that F_ν is not known in advance of solving the problem, requiring iterations, or other approximations.

We can now write the LTE gray-atmosphere solution and compare numerical results with temperatures in the Earth's atmosphere. Equation (1.2.38) gives a solution, similar to (1.2.32),

$$T^4(\tau) = T_0^4(1 + \tfrac{3}{2}\tau) \tag{1.2.43}$$

where T_0 is the temperature of the upper boundary. Here the integrated black-body intensity is

$$B(\tau) = \frac{\sigma}{\pi} T^4(\tau) \tag{1.2.44}$$

The total radiant flux from the Earth can be expressed in terms of a *mean planetary emission temperature*, obtained by integrating Eq. (1.2.31) over frequency:

$$T_e^4 = 2T_0^4 \tag{1.2.45}$$

For a rotating planet of radius R at a uniform temperature over the sphere this temperature is related to the incident solar flux by

$$4\pi R^2 \sigma T_e^4 = (1 - \Lambda)\pi R^2(\pi \mathscr{F}_\odot) \tag{1.2.46}$$

where Λ is the effective planetary albedo and $\pi\mathscr{F}_\odot$ is the incident solar flux. With $\Lambda = 0.29$ for Earth, we find $T_e = 255°\text{K}$ and a boundary temperature $T_0 = T_e/1.19 = 215°\text{K}$, which is close to the mid-latitude tropopause temperature. If we know the optical thickness of the atmosphere versus height, we can figure the temperature versus height—the lapse rate for radiative equilibrium. An example is given in Problem 1.3.

The discontinuity between the air and surface temperature can be expressed from (1.2.29) as

$$\begin{aligned} T_s^4 &= T^4(\tau_g) + \tfrac{1}{2}T_e^4 \\ &= T_0^4(2 + \tfrac{3}{2}\tau_g) \\ &= T_e^4(1 + \tfrac{3}{4}\tau_g) \end{aligned} \tag{1.2.47}$$

where τ_g is the optical thickness at the ground. The deposition of sunlight striking the Earth is shown in Table 1.1.

Equations (1.2.43) and (1.2.47) illustrate how high temperatures can be attained near the ground if the infrared τ is large and heating is from below.

TABLE 1.1 *Approximate Percentage Deposition of Incident Solar Flux*[a]

Reflected to space	Absorbed by ground	Absorbed in troposphere	Absorbed above troposphere	Reradiated from ground to atmosphere
40	40	18	2	25

[a] The solar constant outside the atmosphere is 2 cal/min cm^2 = 1.39 × 10^6 erg/cm^2 sec; the global average heat received is one fourth this amount.

Heating from this combination of a transparent atmosphere in the visible, where the sun's energy is a maximum, and of high opacity in the infrared, where the Earth's Planckian curve peaks, is known as the *greenhouse effect*. It has long been thought that the trapping of infrared by glass is not the important thing in warming greenhouses. Rather, it is said, the glass roof merely keeps the warm air from convecting away. Purists have fought a steadily losing battle to replace "greenhouse effect" with a less picturesque term. We prefer to think of atmospheres as warming by the greenhouse effect, even if greenhouses do not.

If there is no internal heat source, the emission temperature T_e, computed from (1.2.46), will be equivalent to the measured *bolometric temperature* T_b, which is obtained by measuring the mean planetary flux from thermal emission over all frequencies and setting it equal to σT_b^4. In the case of Jupiter and possibly other major planets, $T_b > T_e$, indicating internal generation of heat (cf. Section 1.8.3).

If an atmosphere's thermal emission is measured only in a narrow frequency interval, its intensity gives a *brightness temperature* T_B, defined by $I_\nu = B_\nu(T_B)$. If the atmosphere were gray, I_ν would be Planckian and T_B would be the same at all frequencies and the same as T_b. The brightness temperature of Venus in the microwave spectrum gave the first indication of its 750°K surface (cf. Section 1.8.1).

1.3 Convection in the Troposphere

As we have seen, a gray atmosphere in radiative equilibrium approaches a finite "skin temperature" at high altitude. This isothermal region is stable against convective circulation. At large τ, however, the radiative gradient dT/dz becomes steep (i.e., negatively large). Hence, an optically thick, gray atmosphere can be convectively unstable at low altitudes; the temperature distribution that radiative exchange tends to establish is then too steep to be hydrostatically supported.

If an element of gas moves adiabatically, the first law of thermodynamics requires that

$$C_v\,dT = -p\,dV \tag{1.3.1}$$

where C_v is the specific heat at constant volume (erg/gm°K). If V is the *specific volume* containing a gram of molecules, then the perfect gas law gives

$$dV = \frac{N_0 k}{p} dT - \frac{N_0 kT}{p^2} dp \tag{1.3.2}$$

where $N_0 = 1/M$ and M is the molecular mass. Since $C_p = C_v + N_0 k$ (erg/gm°K), we have the alternate thermodynamic relation

$$C_p\,dT = \frac{N_0 kT}{p}\,dp = V\,dp = \frac{1}{\rho}\,dp \tag{1.3.3}$$

With hydrostatic equilibrium, (1.1.1), the first law thus gives the *dry adiabatic temperature gradient*,

$$\frac{dT}{dz} = -\frac{g}{C_p} = -\frac{\gamma - 1}{\gamma}\frac{gM}{k} \tag{1.3.4}$$

where $\gamma = C_p/C_v$. For the Earth's troposphere this lapse rate (the negative of the temperature gradient) is 9.8°K/km.

For saturated air the first law includes the latent heat released by water condensing:

$$C_v\,dT = -p\,dV - L\,dw_s, \qquad C_p\,dT = \frac{1}{\rho}\,dp - L\,dw_s \tag{1.3.5}$$

where w_s is the mass of saturated water per mass of air and L is the latent heat of vaporization. The *saturation adiabatic lapse rate* is then

$$-\frac{dT}{dz} = \frac{g/C_p}{1 + (L/C_p)(dw_s/dT)} \tag{1.3.6}$$

The wet lapse rate may be about half the dry rate or around 5°K/km. Since convection is partly moist and partly dry, the troposphere has an average value of 6.5°K/km. This value characterizes the static stability of the Earth's large-scale weather systems (see Section 2.2.4).

The temperature distribution in radiative-convective equilibrium is thus simply the adiabatic curve at low altitudes, merging into the purely radiative one at higher levels (see Fig. 1.5). Of an infinite number of parallel adiabatic atmospheres we must select the one that emits the same upward radiant flux as the radiative atmosphere itself. For example, curve 1 in Fig. 1.5 is tangent to the radiative curve and would not require a temperature discontinuity. But the adiabatic curve is everywhere below the radiative one and it clearly cannot supply the radiant flux required above point A to support the temperature there in radiative equilibrium.

A self-consistent solution is an adiabatic curve displaced to the right by an amount such that the flux boundary condition is satisfied. The temperature discontinuity at the ground must also be removed, since it is unstable convectively. The flux given by the various adiabatic distributions is readily computed from the formal solution to the transfer equation (1.2.16).

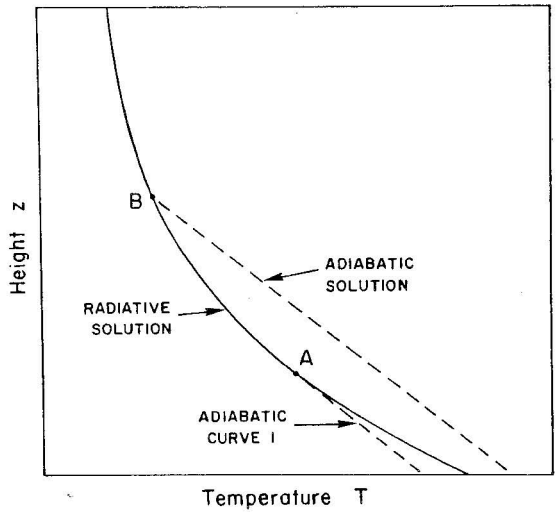

Fig. 1.5 When convection is present the adiabatic portion of the curve not only extends to a point where the radiative solution is convectively stable; it must also supply the thermal radiation to sustain the profile above "*B*." Point *B* is called the *radiative-convective boundary*. The tropopause, defined as the base of the first isothermal region, is just above the top of the figure.

1.4 Latitudinal Variations of the Tropopause and Departures from Grayness

The radiative-convective model with a gray atmosphere reproduces the main features of the troposphere temperature distribution, with the radiative "skin temperature" being identified with the near-isothermal region of the tropopause. This happy state of affairs does not hold, however, when we examine some of the finer features. Figure 1.6 shows isotherms on meridional cross sections for the various seasons. The heavy line shows the location of the tropopause. It is apparent from (1.2.45) and (1.2.46) that in the gray atmosphere, heated from below and without dynamical interchange latitudinally, the tropopause would be warmer in the tropics than in the Arctic simply because the ground temperature is higher. In fact, the tropic tropopause is around 15 km with $T \approx 195$°K, whereas over the polar cap it is as low as 8 to 10 km and $T \approx 225$°K.

Why should the tropopause be lower and warmer in the Arctic? There are several contributing factors. Quite likely the most important is the fact that the atmosphere is not only nongray but the distribution of the infrared active gases (CO_2, H_2O, and O_3) varies with latitude.

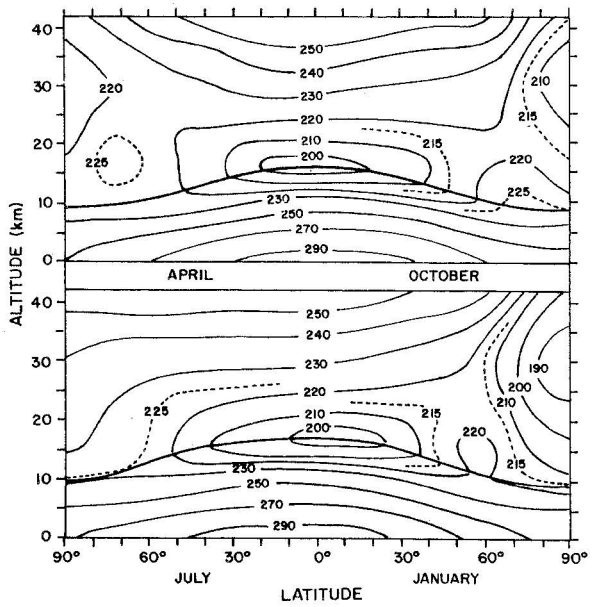

Fig. 1.6 Distribution of the observed temperature (°K) in the northern hemisphere for different seasons. [Based on data assembled by J. LONDON; see MANABE and STRICKLER (1964).]

The departure from grayness itself diminishes the coupling between the ground and skin temperatures. With windows in the absorption spectrum, the ground can cool by radiating directly to space or to the stratosphere. The higher water vapor in the tropics inhibits this direct cooling of the ground but, more important, it increases the cooling of the upper troposphere. This dependence of absolute humidity on air temperature is probably the most important item governing tropopause height.

Another factor is the latitudinal dependence of stratospheric ozone. In a static atmosphere, ozone would be most abundant where it is most readily created—at lower latitudes. In fact (as we shall discuss in Section 3.3.2), it is more abundant at higher latitudes. The 9.6 μm band of O_3 is largely responsible for heating the lower stratosphere by absorbing surface infrared radiation in an otherwise clear window. In addition, we have so far neglected direct heating by the sun, but the existence of the stratosphere is primarily due to direct solar photolysis and heating. With ozone more abundant in the Arctic and distributed more toward low altitudes than in the tropics, it has a different effect on the temperature profile. The tropic tropopause is sharply defined, with an abrupt temperature inversion and rapid rise in the lower stratosphere. In the polar regions the lower stratosphere is nearly

isothermal, and these differences are probably due to the different ozone distributions.

Nevertheless, detailed model calculations have not given as satisfactory agreement as one would desire, suggesting other effects are contributing. The meridional circulation of the stratosphere is known to be important (see Section 3.3.2) and it probably has an influence on the tropopause height and temperature of the lower stratosphere. Also, convection is driven more strongly in the tropics, both because solar radiation is more abundant, and because of the cooling of the upper troposphere by the increased water vapor.

The interplay of all these effects requires elaborate computational models in which one feature is varied at a time to see what its effect is. Often the effects involve such complex feedbacks that the physics at work becomes obscure.

1.5 The Stratosphere: Absorption of Direct Solar Radiation

For an elementary examination of the stratospheric heating, we will oversimplify the problem while retaining enough of the relevant physics to see what is happening. In Chapter 3 the ozone-related chemistry is examined more thoroughly. (Also, the basic principles of photochemistry are reviewed in Section 3.1.) For now let us suppose that the only reactions of importance involve only oxygen: the so-called "Chapman reactions."

1.5.1 Elementary Oxygen Chemistry

Molecular oxygen in the stratosphere is photodissociated by absorption in the Herzberg continuum:

$$O_2 + h\nu \rightarrow O(^3P) + O(^3P) \tag{1.5.1}$$

Atomic oxygen then attaches to O_2 in the presence of an unspecified third body M to form ozone,

$$\begin{gathered} O + O_2 + M \rightarrow O_3 + M \\ k_{12} = 6.0 \times 10^{-34}(T/300)^{-2.3}\ \text{cm}^6/\text{sec} \end{gathered} \tag{1.5.2}$$

where k_{12} is the three-body rate coefficient (see Section 3.1). Both kinds of "odd oxygen" (i.e., O and O_3) are destroyed by

$$\begin{gathered} O + O_3 \rightarrow O_2 + O_2 \\ k_{13} = 8.0 \times 10^{-12} e^{-2060/T}\ \text{cm}^3/\text{sec} \end{gathered} \tag{1.5.3}$$

and O_3 is converted back to O by

$$O_3 + h\nu \rightarrow O + O_2 \tag{1.5.4}$$

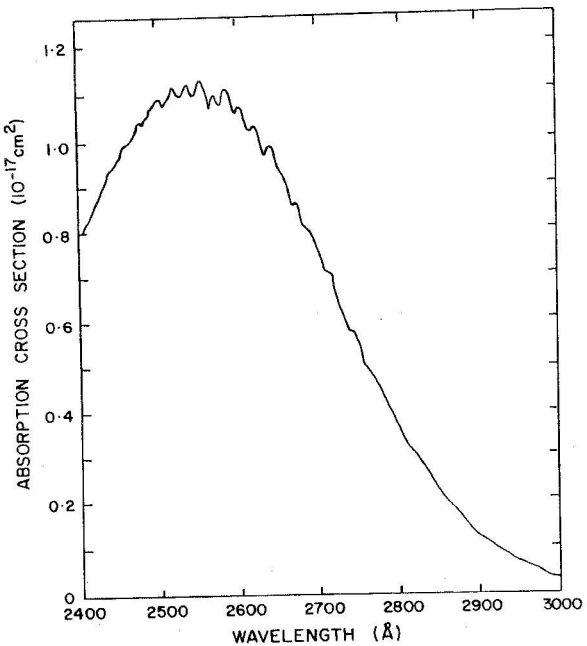

Fig. 1.7 Absorption cross sections of the Hartley bands and continuum. [Measurements by E. C. Y. INN and TANAKA (1953), *J. Opt. Soc. Amer.* **43**, 870.]

The principal source of heating is this O_3 dissociation, which occurs in the strong Hartley continuum, shown in Fig. 1.7. Over this region O_3 is the only atmospheric substance strongly absorbing (Fig. 1.8).

Thus not only is this absorption responsible for heating the stratosphere, but the O_3 there prevents sunlight in the 0.2–0.3 μm region from reaching the ground. Since many forms of life (including the DNA molecule) cannot tolerate the ultraviolet, the 0.3 atm-cm or so in the stratosphere seems a very thin shield indeed. Only because O_3 is a strong absorber in the Hartley region (cross section of 10^{-18}–10^{-17} cm^2) can so few molecules accomplish so much.

The O_2 absorption (1.5.1), on the other hand, is intrinsically very weak. It is important to keep in mind that there are two photodissociation continua for O_2 important in atmospheric physics (cf. Fig. 1.9). The stronger one, the *Schumann–Runge continuum*, lies at wavelengths shortward of 1750 Å (7.1 eV). It involves the electronic transition $B\,^3\Sigma_u^- \leftarrow X\,^3\Sigma_g^-$ and hence is permitted as an electric-dipole transition. The measured cross section is in the range 10^{-18}–10^{-17} cm^2 and O_2 dissociates into $O(^3P) + O(^1D)$, that is, one atom in the ground term and one in the metastable ^1D term at 2 eV. This dissociation occurs in the 100 km region and sunlight at $\lambda < 1750$ Å is totally extinguished above the stratosphere.

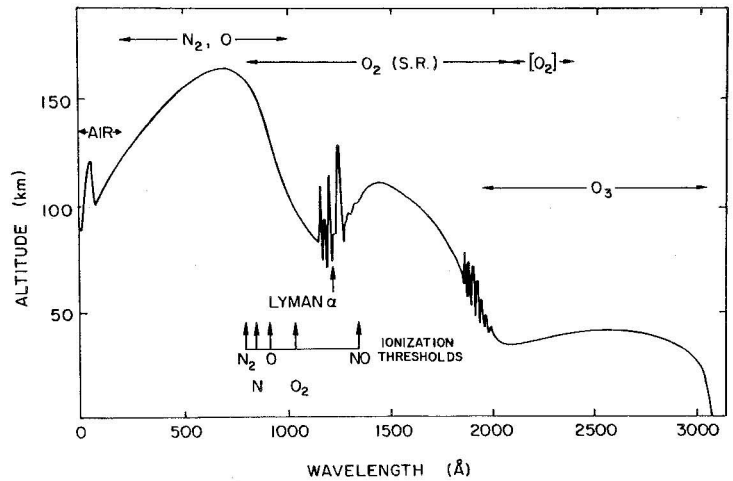

Fig. 1.8 Altitude at which the intensity of solar radiation drops to $1/e$ of its value outside Earth's atmosphere for vertical incidence. The Schumann–Runge and forbidden Herzberg O_2 absorbing regions are denoted by S.R. and [O_2], respectively. [Based on data assembled in 1961 by P. J. NAWROCKI, K. WATANABE, and L. G. SMITH; adapted from L. HERZBERG (1965), *in* "Physics of the Earth's Upper Atmosphere" (C. W. Hines *et al.*, eds.), p. 40, Prentice-Hall, Englewood Cliffs, New Jersey.]

The weaker absorption occurs at $\lambda < 2420$ (5.1 eV). It involves the forbidden Herzberg continuum $A\,^3\Sigma_u^+ \leftarrow X\,^3\Sigma_g^-$ whose cross section is 10^{-24}–10^{-23} cm^2, and the dissociation products are both in the ground term $O(^3P)$.

When the source function (representing local scattering or emission) is negligible, the transfer equation (1.2.11) gives the absorption per unit volume as

$$\mu \frac{dI_\nu(z)}{dz} = -\kappa_\nu \rho I(z) \tag{1.5.5}$$

$$\mu \frac{dI_\nu(z)}{dz} = -\kappa_\nu \rho I_\nu(\infty) e^{-\tau_\nu/\mu} \tag{1.5.6}$$

We will pursue this equation further in discussing the formation of the ionosphere (Section 5.1.1), but for the moment we will simply note that, in a barometric atmosphere (1.4), the maximum absorption occurs at (see Problem 1.4).

$$\tau_\nu/\mu = \kappa_\nu \rho H/\mu = \alpha_\nu N(z) H/\mu = 1 \tag{1.5.7}$$

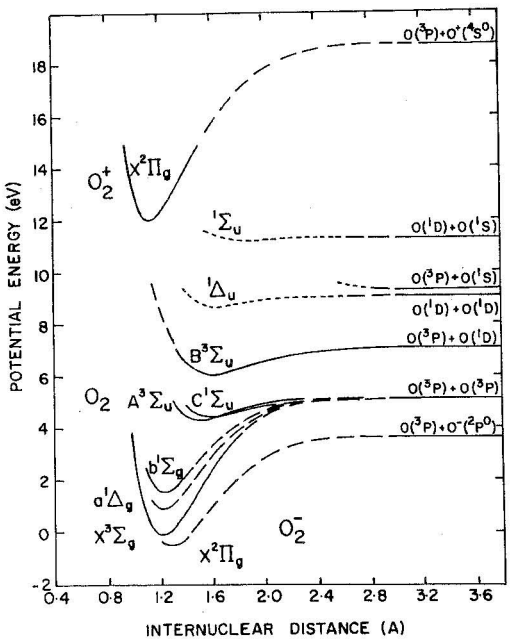

Fig. 1.9 Simplified potential energy diagram for oxygen. Along the right side are listed the dissociation products; an energy level diagram of O appears as Fig. 6.3.

where α_ν (cm^2) is the molecular cross section. Hence the Schumann–Runge dissociation peaks near 100 km; the Herzberg dissociation would peak in the 20–25 km region, except that O_3 absorption between 1800 and 2400 Å raises the $\tau_\nu = 1$ level to about 40 km. The actual absorption coefficients are not gray and the destruction of O_3, involving reactions (1.5.2), (1.5.3), and (1.5.4), places the maximum ozone abundance somewhat lower, around 25–30 km altitude.

We can make an approximate assessment of the ozone distribution with the above four equations in daytime photochemical equilibrium. First, O is created by dissociation (1.5.1) at a rate $2J_2(z)$ (sec^{-1} per O_2 molecule), which depends on the photon flux (cm^{-2} sec^{-1}) of dissociating radiation at height z and the O_2 absorption cross section (cm^2) in the Herzberg continuum. Similarly (1.5.4) proceeds at rate J_3 (sec^{-1} per O_3 molecule). The destruction of O by the two-body reaction (1.5.3) is given by the rate coefficient k_{13} (cm^3/sec), which is the mean of the O–O_3 association cross section times the velocity of collision. Cross sections for chemical reactions may have a strong velocity dependence, making the rate coefficients strongly temperature dependent. Finally, the three-body reaction (1.5.2) has a rate coefficient k_{12} (cm^6/sec). Rate coefficients are discussed more thoroughly in Section 3.1.

Thus the net change in O abundance is

$$\frac{d[O]}{dt} = 2J_2(z)[O_2] + J_3(z)[O_3] - k_{13}[O][O_3] - k_{12}[O][O_2][M] \quad (1.5.8)$$

where brackets denote concentrations (molecule/cm^3). Similarly, the O_3 rate of change is

$$\frac{d[O_3]}{dt} = k_{12}[O][O_2][M] - k_{13}[O][O_3] - J_3[O_3] \quad (1.5.9)$$

In chemical equilibrium these two equations lead to

$$[O] = \frac{J_2[O_2]}{k_{13}[O_3]} \quad (1.5.10)$$

and

$$[O_3] = \frac{k_{12}[O][O_2][M]}{k_{13}[O] + J_3} \quad (1.5.11)$$

Below 60 km the term $k_{13}[O] \ll J_3$ because of the low O abundance. Then we have

$$\frac{[O_3]_{day}}{[O_2]} \approx \left(\frac{k_{12}J_2[M]}{k_{13}J_3}\right)^{1/2} \quad (1.5.12)$$

and

$$[O]_{day} \approx \left(\frac{J_2J_3}{k_{12}k_{13}[M]}\right)^{1/2} \quad (1.5.13)$$

The daytime distribution of oxygen allotropes is shown in Fig. 1.10. At nighttime O_3 grows at the expense of O through (1.5.2), which proceeds rapidly because O_2 is large. Nevertheless, since $[O] \ll [O_3]$ in the stratosphere, the resulting increase in O_3 is relatively small. Were there a plentiful supply of O, the nighttime equilibrium of O_3 would grow to

$$\frac{[O_3]_{night}}{[O_2]} \to \frac{k_{12}[M]}{k_{13}} \quad (1.5.14)$$

but in the stratosphere the O rapidly disappears at night and the O_3 becomes essentially inert.

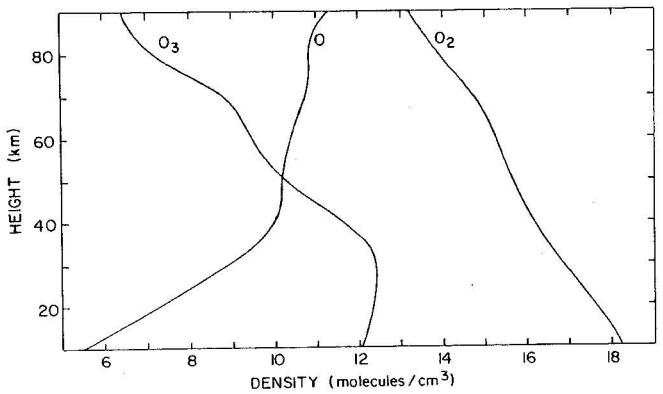

Fig. 1.10 Daytime equilibrium of oxygen allotropes according to the Chapman theory. The abscissa is $\log_{10} N$. [Calculations by D. R. BATES (1954) *in* "The Earth as a Planet" (G. P. Kuiper, ed.), p. 581, Univ. Chicago Press, Chicago.]

1.5.2 Stratospheric Heating

A calculation of the stratospheric temperature profile is not a simple task even with simplified photochemistry, the absence of vertical mixing, and ignored meridional dynamics. While the solar heating is not too complicated (although the solar-energy input at each level must be averaged over the day for any latitude and time of year) the infrared net cooling (or heating) is less straightforward. For example, weak rotational lines in the 15 μm fundamental band of CO_2 and lines in isotopic bands and weak *hot bands* (which arise from an excited lower vibrational level) are important in radiating directly to space, whereas stronger transitions in CO_2, H_2O, and O_3 provide a complex interchange of radiation within the atmosphere. The problem can be handled only by intricate computer codes.

With it understood that these complexities are being greatly oversimplified, we can at least examine the fundamental physics of solar heating. The Herzberg O_2 continuum is screened by not only the overhead O_2 but by O_3. Hence we have

$$J_2(z) = J_2^{(0)} \exp\left(-\frac{\tau_2(O_2, z)}{\mu} - \frac{\tau_2(O_3, z)}{\mu} \right) \tag{1.5.15}$$

where $J_2^{(0)}$ is the value outside the atmosphere. The extinction due to O_2 is

$$\tau_2(O_2, z) = \alpha_2(O_2) \int_z^\infty [O_2(z)]\, dz \tag{1.5.16}$$

and that due to O_3 is

$$\tau_2(O_3, z) = \alpha_2(O_3) \int_z^\infty [O_3(z)]\, dz \tag{1.5.17}$$

The extinction of $J_3(z)$ is similarly defined by

$$\tau_3(O_3, z) = \alpha_3(O_3) \int_z^\infty [O_3(z)]\, dz \tag{1.5.18}$$

where α_3 is the average absorption cross section in the Hartley continuum.

The evaluation of (1.5.12) for $[O_3]$ thus involves $[O_3]$ on the right-hand side, but we may proceed by successive approximations. Let us begin by making the obviously crude assumption that all constituents follow the same atmospheric scale height H. Then (1.5.12) gives for a first approximation

$$\frac{[O_3(z)]_{\text{day}}}{[O_2(z)]} \approx \left(\frac{k_{12}[M(z_0)]J_2^{(0)}}{k_{13}J_3^{(0)}} \right)^{1/2} e^{-(z-z_0)/2H} \exp\left(-\frac{\tau_0}{2\mu} e^{-(z-z_0)/H} \right) \tag{1.5.19}$$

where

$$\tau_0 = \tau_2(O_2, z_0) + \tau_2(O_3, z_0) - \tau_3(O_3, z_0) \tag{1.5.20}$$

Equation (1.5.19) has the form of a so-called "Chapman layer," which we will encounter again in ionosphere theory (see Section 5.1.1). The simple exponential represents diminished absorption with increasing altitude simply because of the decreasing abundance of the absorber. The compound exponential is due to attenuation of sunlight, which causes the "layer" to diminish deep in the atmosphere. The relative abundance of $[O_3]$ would, in this approximation, peak at $\tau_0/\mu = 1$; that is, at the τ_0 "absorption" peak [see Eq. (1.5.6)]. The absolute $[O_3]$ peak, however, is at $\tau_0/\mu = 3$, or well below the τ_0 "absorption" peak. The reader should be aware that (1.5.19) is a poor approximation for a real ozone layer since τ_0 itself depends on $[O_3]$.

The instantaneous heating rate from dissociation is then

$$\left(\frac{dT}{dt} \right)_{\text{heat}} = \frac{[O_2(z)]}{\rho(z) C_p} \left(J_2(z) h\nu_2 + J_3(z) h\nu_3 \frac{[O_3(z)]_{\text{day}}}{[O_2(z)]} \right) \tag{1.5.21}$$

where $\rho(z)$ is the local mass density, C_p is the specific heat of air (erg/gm°K), and ν_2 and ν_3 are average frequencies of the O_2 Herzberg and O_3 Hartley continua, respectively. It is a good approximation to assume that all the solar energy absorbed in the stratosphere goes into heating. Part of it appears as kinetic energy at the moment of dissociation; part goes into metastable states, such as $O(^1D)$, and is collisionally deactivated (i.e., transformed into heat); and part (the dissociation energy itself) appears as heat when the dissociation products react chemically to re-associate by (1.5.2) and (1.5.3).

To find the equilibrium temperature we equate the heat absorbed to that emitted. At high altitudes the infrared region of the atmosphere becomes

optically thin and radiates directly to space. This assumption is occasionally used to examine small fluctuations in heating and temperature and is called the *transparent approximation.* Assuming grayness for the emitting gases, we have [cf. (1.2.44)]

$$4\pi\kappa B(z) \equiv 4\kappa\sigma T^4 = C_p\left(\frac{dT}{dt}\right)_{\text{cool}} \tag{1.5.22}$$

where κ (cm^2/gm) is the absorption coefficient. The actual atmosphere is far from gray and a *linear* or *Newtonian* law of cooling is often adopted:

$$C_p\left(\frac{dT}{dt}\right)_{\text{cool}} = aT \tag{1.5.23}$$

where a is a constant ($\sim 4\kappa\sigma T_0{}^3$). An example of the use of these simplified equations is given in Problem 1.6. The average overhead absorption for atmospheric gases in the infrared is shown in Fig. 1.11.

1.5.3 Water in the Stratosphere

The predominant carrier of radiative energy in the troposphere is H_2O, although CO_2 is also important, especially at higher altitudes. In the stratosphere and above, H_2O is much less important owing to its small mixing

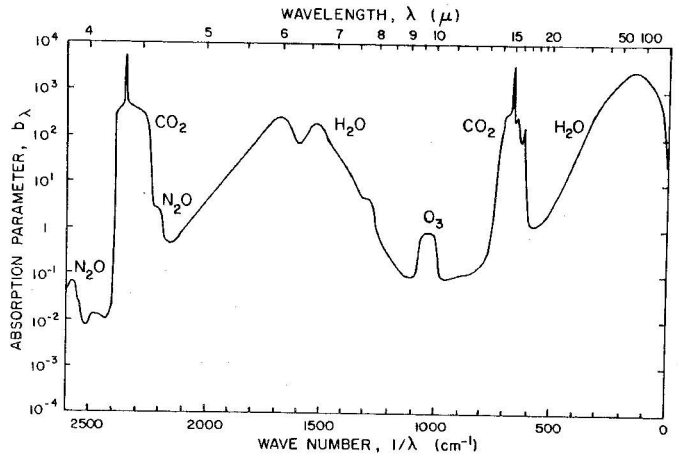

Fig. 1.11 An indication of the absorbing properties of the lower atmosphere is b_λ, where $1/b_\lambda$ is the thickness in atmospheres that would give 50 percent absorption and 50 percent transmission. In this limited sense, b_λ is a kind of optical thickness, even though over finite wavelength intervals the atmosphere does not absorb according to the Lambert exponential-attenuation law (1.2.2). [Adapted from C. W. ALLEN (1973), "Astrophysical Quantities," 3rd ed., p. 130, Athlone Press, London.]

ratio. The mixing ratio of stratospheric H_2O is about 5×10^{-6} by volume and this amount would produce a saturated vapor pressure at the low temperature of the tropical tropopause ($\sim$195°K at 15 km). Hence it is commonly thought that the tropopause acts as a kind of cold trap. Any higher fraction of water would eventually find condensation nuclei, condense as ice, and fall out.

1.6 The Mesopause: Vibrational Relaxation of CO_2

Above the stratosphere the heating is mainly due to the absorption of solar ultraviolet by ozone and CO_2 absorption at 15 μm; the latter band also dominates the cooling. The ratio $[O_3]/[CO_2]$ diminishes slowly with increasing altitude, and the ratio of heating to cooling does the same. The temperature thus monotonically decreases at an average gradient of about -5°K/km, quite stable in comparison with the dry adiabatic gradient (1.3.4) of -9.8°K/km.

The direct absorption of sunlight is thus small, and radiation transport, primarily in the 15 μm band of CO_2, becomes dominant in governing the temperature distribution.

1.6.1 The CO_2 ν_2 Fundamental Transition

The CO_2 molecule is linear (see Fig. 1.12). Consequently, the ν_1 mode, symmetric vibration, has no dipole moment for $^{16}O^{12}C^{16}O$, and the vibration-rotation spectrum is absent, just as it is for homonuclear diatomic molecules. The ν_2 or bending mode has the lowest fundamental, occurring at 667.3 cm^{-1} or 15 μm. The ν_2 degeneracy (meaning the energy is equivalent for a vibration in the plane of the page and one perpendicular to it) is removed with rotation. Hence the transition is formally written $(0\,1^1\,0) \leftrightarrows (0\,0^0\,0)$,

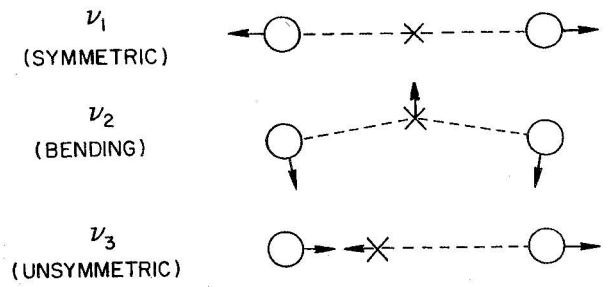

Fig. 1.12 Vibrational modes for the linear OCO molecule.

where the principal numbers are the three vibrational quantum numbers v_i, and where the superscript is l, the quantum number specifying the *angular momentum of vibration* ($0 \leq l \leq v_2$). The v_3 mode, unsymmetric vibration, is $(0\,0^0\,1) \leftrightarrows (0\,0^0\,0)$, which occurs at 2350 cm^{-1} or 4.3 μm and is an order of magnitude stronger in absorption. But because the 15 μm band is more readily excited at the low mesospheric temperatures, is strong enough to be optically thick, and remains in local thermodynamic equilibrium (LTE) with the atmosphere to higher altitudes, it is the more important. The latter point requires some discussion, for the breakdown of LTE occurs through the phenomenon of *vibrational relaxation.*

1.6.2. Kirchhoff's Law and Vibrational Relaxation

In treating radiation in the troposphere (see Section 1.2.3), where many substances (e.g., H_2O, CO_2) are radiatively active, we adopted a gray-atmosphere approximation for the infrared. Now we are concerned with a single vibrational transition for transporting heat, and it might seem that the use of Kirchhoff's law is no longer appropriate. We will demonstrate here that the approaches of thermodynamics and molecular physics are equivalent.

First, assume there is no scattering. The emitted radiation (erg/cm^3 sec sr Hz) from unit volume is given by the emission coefficient of (1.2.1),

$$dI_\nu/ds = \rho j_\nu \tag{1.6.1}$$

where by (1.2.6), $j_\nu = \kappa_\nu B_\nu$. Integrating over the band profile (which we cannot now regard as gray but must represent with a realistic κ_ν variation), we have an omnidirectional emission of energy density E in the entire $v' = 1 \rightarrow v = 0$ band of

$$\frac{dE(1,0)}{dt} \equiv \int_{\text{sphere}} \int_{\text{band}} \frac{dI_\nu}{ds}\, d\nu\, d\Omega = 4\pi\rho B_\nu \int_\nu \kappa_\nu\, d\nu \tag{1.6.2}$$

where B_ν comes out of the integrals since we are concerned with isotropic emission over a small frequency interval wherein $B_\nu \approx$ const. Making use of the identity

$$\rho\kappa_\nu = N(v)\alpha_\nu(v, v') \tag{1.6.3}$$

to write the absorption coefficient in terms of the molecular cross section $\alpha_\nu(v, v')$, and the CO_2 population in the lower vibrational level $N(v)$, we have

$$\frac{dE(1,0)}{dt} = \frac{4\pi N(0) 2h\nu^3}{c^2(e^{h\nu/kT} - 1)} \int \alpha_\nu(0,1)\, d\nu \tag{1.6.4}$$

The integrated absorption cross section is expressed commonly in a variety of equivalent ways, including the *band strength* S, the *oscillator strength* f, the Einstein *absorption coefficient* B, or (since the three Einstein coefficients are uniquely related) the emission *transition probability* A. Thus we may choose from

$$\begin{aligned} \int \alpha_\nu(0,1)\, d\nu &= S(0,1) \\ &= \frac{\pi e^2}{mc} f(0,1) \\ &= \frac{h\nu}{4\pi} B(0,1) = \frac{c^2}{8\pi\nu^2} \frac{\tilde{\omega}(1)}{\tilde{\omega}(0)} A(1,0) \end{aligned} \tag{1.6.5}$$

where $\tilde{\omega}$ represents the *statistical weight* of a level. Opting for the transition probability, we write

$$\frac{dE(1,0)}{dt} = \frac{N(1)A(1,0)h\nu}{1 - e^{-h\nu/kT}} \text{ erg/cm}^3\,\text{sec} \tag{1.6.6}$$

since in thermodynamic equilibrium the relative populations of levels v and v' are given by Boltzmann's excitation equation,

$$\frac{N(v')}{N(v)} = \frac{\tilde{\omega}(v')}{\tilde{\omega}(v)} \exp\left(-\frac{h\nu(v'v)}{kT}\right) \tag{1.6.7}$$

For a diatomic molecule we can regard the vibrational levels (summed over all rotational levels) as having the same statistical weights, $\tilde{\omega}(v') = \tilde{\omega}(v)$.

From the approach of molecular physics, the rate of energy emission from $v' = 1 \rightarrow v = 0$ is

$$\frac{dE(1,0)}{dt} = N(1)[A(1,0) + B_\nu(T)B(1,0)]h\nu \tag{1.6.8}$$

where $B(1,0)$ is the *Einstein coefficient for stimulated emission*, and we take the incident intensity as Planckian and characteristic of the local temperature. The Einstein relationships are

$$\tilde{\omega}(1)B(1,0) = \tilde{\omega}(0)B(0,1) = \frac{\tilde{\omega}(1)c^2}{2h\nu^3} A(1,0) \tag{1.6.9}$$

With B_ν given by (1.2.7), Eq. (1.6.8) reduces to (1.6.6).

Of course, it is scarcely surprising that the two approaches are equivalent when one considers that we have assumed Planckian radiation and a Boltzmann distribution of level populations. These conditions are, after all, used to establish the relationships among the Einstein A and B's. Conversely, if the radiation field is far from isotropic or not characteristic of the local

temperature or if collisions are not frequent enough to maintain the Boltzmann distribution (1.6.7), the Kirchhoff relationship does not apply and we must look at the molecular physics to ascertain the emission.

Let us examine the collision and radiation physics to see when thermodynamic equilibrium becomes a poor approximation. Radiation is transferred to heat by absorption,

$$CO_2(v = 0) + h\nu \rightarrow CO_2(v' = 1) \tag{1.6.10}$$

followed by collisional deactivation,

$$CO_2(v' = 1) + M \rightarrow CO_2(v = 0) + M + \text{K.E.} \tag{1.6.11}$$

where K.E. ($= h\nu$) is the kinetic energy supplied to the gas. The rate coefficient for deactivation is $\eta(1,0)$ (cm^3/sec) so that

$$\frac{d[CO_2(1)]}{dt} = -[CO_2(1)][M]\eta(1,0)\ \text{cm}^{-3}\ \text{sec}^{-1} \tag{1.6.12}$$

On the other hand, absorption by (1.6.10) may be followed by spontaneous emission,

$$CO_2(v' = 1) \rightarrow CO_2(v = 0) + h\nu \tag{1.6.13}$$

in which case there is no radiation transferred into kinetic energy and the combination (1.6.10) plus (1.6.13) amounts to scattering. Neglecting the small stimulated-emission term in the denominator of (1.6.6), the loss of $CO_2(v' = 1)$ by spontaneous emission is

$$\frac{d[CO_2(1)]}{dt} = -[CO_2(1)]A(1,0) \tag{1.6.14}$$

which gives an albedo for single scattering of

$$\tilde{\omega}^* = \frac{A(1,0)}{A(1,0) + \eta(1,0)[M]} \tag{1.6.15}$$

which is independent of frequency within the 1-0 band.

The equation of transfer (1.2.11), with (1.2.14) and (1.2.17), is then

$$\mu \frac{dI_\nu}{d\tau_\nu} = I_\nu - \tilde{\omega}^* J_\nu - (1 - \tilde{\omega}^*)B_\nu \tag{1.6.16}$$

When $\tilde{\omega}^* \approx 0$ the coupling of the gas to the radiation field is strong; this is the state of LTE. But when $\tilde{\omega}^* \approx 1$, the upper state scatters the incident photons and the kinetic temperature of the gas is not strongly affected by the incident radiation.

The shift from $\tilde{\omega}^* \approx 0$ to $\tilde{\omega}^* \approx 1$ is called *vibrational relaxation* [meaning that vibrational populations are no longer governed by the Boltzmann

equation (1.6.7)], and it occurs at

$$[M] \lesssim \frac{A(1,0)}{\eta(1,0)} \tag{1.6.17}$$

For the ν_2 band of CO_2, the band strength is $S(0,1) = 2.37 \times 10^{-7}$ cm^2/sec, giving $A(1,0) = 1.35\ \text{sec}^{-1}$. Adopting $\eta(1,0) = 2.5 \times 10^{-15}$ cm^3/sec, we find relaxation occurs for densities $[M] \lesssim 10^{15}$ cm^{-3}, which occurs around 70–75 km.

Above this altitude radiative absorption is negligible compared with collisional excitation, although the gas still radiatively cools by emission of energy at the rate

$$\frac{dE(1,0)}{dt} = \eta(0,1)\tilde{\omega}^*[M][CO_2]h\nu \tag{1.6.18}$$

where the excitation rate coefficient is related to the deactivation coefficient (through thermodynamic considerations of detailed balancing) by

$$\tilde{\omega}(0)\eta(0,1) = \tilde{\omega}(1)\eta(1,0)e^{-h\nu/kT} \tag{1.6.19}$$

When the relative populations are not in thermodynamic equilibrium, they must in general be determined by the relative importance of collisions and the radiation field. If the local kinetic temperature is T and radiation characteristic of some other temperature T_0 is incident from below, the excitation is

$$\frac{N(1)}{N(0)} = \frac{\tilde{\omega}(1)}{\tilde{\omega}(0)}\left((1 - \tilde{\omega}^*)e^{-h\nu/kT} + \frac{\tilde{\omega}^*}{2}e^{-h\nu/kT_0}\right) \tag{1.6.20}$$

in lieu of the Boltzmann equation (1.6.7). The $\frac{1}{2}$ factor enters because the gas is irradiated only from below; the equation is based on negligible induced emission (see Problem 1.9).

The temperature of the upper mesosphere will thus decrease upwards until heating from the thermosphere offsets the radiant losses. To estimate where this occurs we must first look at the thermospheric processes.

1.7 Ionization, Dissociation, and Heat Transfer in the Thermosphere

Above 80 km in the Earth's atmosphere the direct absorption of solar energy again becomes important for two reasons: Photoionization, at the lower altitudes mainly by X-rays, and photodissociation in the Schumann–Runge continuum of O_2. (The principles of photochemistry are reviewed in Section 3.1.)

1.7.1 Absorption of Sunlight

The heating that occurs from photoionization involves a number of processes. First is ejection of the electron itself. For an example, let us take the O_2 molecule, although N_2, O, and minor constituents are also ionized by X-rays and NO is ionized by the strong solar Ly α emission of hydrogen at 1215 Å. Thus photoionization,

$$O_2 + h\nu \rightarrow O_2^+ + e \tag{1.7.1}$$

where the ionization potential is about 12 eV and the electron carries away additional kinetic energy. This energy is fed into the neutral gas by collisions that excite electronic states or high vibrational levels. A small amount of the energy is lost to space by molecular radiation, but N_2 and O_2 have no vibrational-rotational spectra, since they are *homonuclear* and have no dipole moment. Hence the excitation energy is converted to kinetic energy by energy exchange,

$$O_2(v') + M \rightarrow O_2(v < v') + M \tag{1.7.2}$$

or, through atom-atom interchange,

$$O_2(v') + O \rightarrow O + O_2(v < v') \tag{1.7.3}$$

How the energy of ionization is converted to heat depends somewhat on the altitude. Below the 90 km region recombination occurs through (a) *electron attachment* to a neutral molecule followed by (b) *mutual neutralization*, a collision between a negative and a positive ion that leaves neutral products. Most of the ionization potential is thus released in the same region where ionization occurs.

At higher altitudes negative ions do not form readily and the positive charge is predominantly on O^+, O_2^+, or NO^+. However, O^+ is very slow to recombine and sooner or later loses its charge to a molecule. Recombination is rapid for charged molecules, proceeding by, for example,

$$O_2^+ + e \rightarrow O + O \tag{1.7.4}$$

dissociative recombination.

Thus the difference between the ionization energy ($\sim$12 eV) and the dissociation energy ($\sim$5 eV) is released in the ionization region, but the reassociation energy is released lower, in the 100 km region, where oxygen associates by

$$O + O + M \rightarrow O_2 + M \qquad k_{11} = 2.76 \times 10^{-34} e^{710/T} \tag{1.7.5}$$

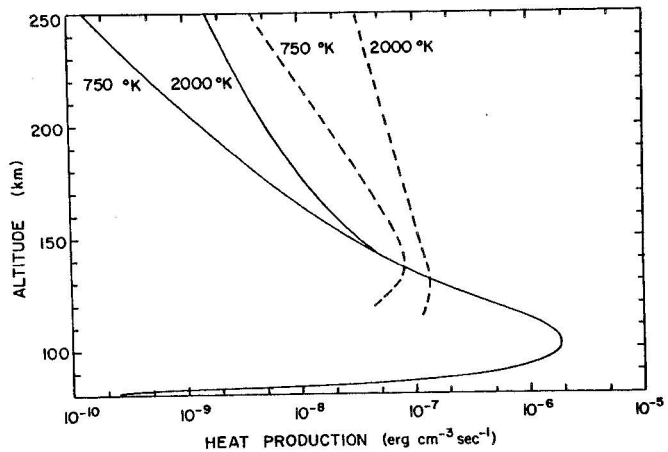

Fig. 1.13 Deposition of heat in the upper atmosphere for an overhead sun ($\mu = 1$) and heating efficiency $\varepsilon = 0.3$, computed for two models having temperatures in the high thermosphere and exosphere of 750 and 2000°K. The curves give the second term on the right of (1.7.19). Solid curves—Schumann–Runge continuum; dashed curves—ionization by $\lambda < 1026$ Å. [Calculations by P. M. BANKS and G. KOCKARTS (1973), "Aeronomy," **B**, p. 19, Academic Press, New York.]

In the same way O_2 is dissociated in the Schumann–Runge continuum and somewhat higher in altitude than the main level of re-association. The vertical interchange of matter, either by molecular diffusion, large-scale wind systems, or eddy mixing, thus plays a significant role in the heat deposition. Figure 1.13 shows heating rates computed for two assumed temperature and density distributions. The Schumann–Runge region is important in the lower thermosphere, and the 80–1026 Å interval that produces ionization dominates in the middle and upper thermosphere. The heating efficiency was taken as 30 percent. The remainder of the incident energy is either radiated away or transported downward in the form of chemical energy to the region where O atoms readily associate.

1.7.2 Oxygen Chemistry and Distribution in the Thermosphere

The strong Schumann–Runge continuum (see Section 1.5.1) at $\lambda < 1750$ Å produces

$$O_2 + h\nu = O(^3P) + O(^1D) \tag{1.7.6}$$

with $J_2(\infty) \sim 4 \times 10^{-6}$ sec^{-1}. The $O(^1D)$ term lies 1.96 eV above ground. It is the upper term of the red 6300 and 6364 Å forbidden lines that appear in

both the airglow and aurora. Association occurs in the presence of a third body by (1.7.5) and by *radiative association*,

$$O + O \rightarrow O_2 + h\nu \tag{1.7.7}$$

although the latter is unimportant compared with the three-body process except well above the main dissociation region. Neglecting (1.7.7) we have an equilibrium distribution of

$$\frac{[O]}{[O_2]} = \left(\frac{J_2}{k_{11}[O_2][M]}\right)^{1/2} \tag{1.7.8}$$

However, the diffusive separation of gases becomes important in the same region (around 100–110 km) where dissociation peaks. The theoretical time for uniformly mixed O_2 and O to approach diffusive equilibrium at 115 km is about 10 days, which is also the lifetime of an O_2 molecule against photodissociation. But in the 100–115 km region, the ratio $[O_2]/[O] \approx \frac{1}{3}$ and is nearly constant. Hence the characteristic time for the lower thermosphere to become thoroughly mixed, from large scale circulation and turbulence, may also be the order of 10 days, with diffusion, mixing, and O_2 photolysis having comparable time scales. In the next chapter we discuss diffusion and mixing more thoroughly. For now we note that somewhere between 115 and 150 km the diffusion time (which varies as the density) becomes sufficiently short that mixing is overcome and O_2, O, and N_2 are all in diffusive equilibrium, meaning that each gas follows hydrostatic equilibrium, (1.1.5), independently for its own mass M_j. The atmospheric scale height is then (cf. Problem 1.1)

$$H = \left(\sum_j \frac{N_j/N}{H_j}\right)^{-1} \tag{1.7.9}$$

where $H_j = kT/M_j g$.

There is no N_2 continuum where solar ultraviolet radiation is strong enough to dissociate it, but N atoms are formed through photoionization,

$$N_2 + h\nu \rightarrow N_2^+ + e \tag{1.7.10}$$

which occurs for $\lambda < 796$ Å, followed by dissociative recombination,

$$N_2^+ + e \rightarrow N + N \tag{1.7.11}$$

Once formed, N can re-associate by the three-body process, but it also reacts with oxygen, forming nitric oxide by

$$N + O + M \rightarrow NO + M \tag{1.7.12}$$

and

$$N + O_2 \rightarrow NO + O \tag{1.7.13}$$

which is very slow at 300°K. However, ion-neutral reactions are the dominant source of N atoms,

$$N_2^+ + O \rightarrow NO^+ + N \tag{1.7.14}$$

$$O^+ + N_2 \rightarrow NO^+ + N \tag{1.7.15}$$

and

$$O_2^+ + N_2 \rightarrow NO^+ + NO \tag{1.7.16}$$

although the latter reaction is probably very slow. Dissociative recombination of NO^+ yields the N atom preferentially in the ^2D state.

A different type of production mechanism involves $N(^2D)$ formed by recombination, (1.7.11). The ^2D term is metastable, at 2.37 eV above ground, $N(^4S)$. Once formed it can react with O_2,

$$N(^2D) + O_2 \rightarrow NO + O(^3P) \tag{1.7.17}$$

Nitric oxide formed in the thermosphere is important to the formation of the lower ionosphere, and we shall return to it in Chapter 5.

1.7.3 Radiative Exchange and Loss

Some of the processes mentioned above emit radiation as they occur. Electron attachment to form a negative ion may proceed either by emitting a stabilizing photon or in the presence of a third body. *Three-body association*, (1.7.5), may leave O_2 in the ground state, $X\,^3\Sigma_g^-$, but it can just as well associate into one of the other (excited) states that correspond to two ground-term $O(^3P)$ atoms (see Fig. 1.9). In that case the excited molecule might emit radiation in one of the O_2 band systems observed in the airglow (see Section 6.1.2), and this loss represents energy not available for thermospheric heat.

The net heating efficiency must also include the loss of infrared radiation due to thermal collisions, such as the CO_2 loss above its level of vibrational relaxation. But the abundant molecules N_2 and O_2 are forbidden to radiate in the infrared by electric-dipole transitions and the minor constituents that can radiate (NO, CO, etc.) are rare in the Earth's atmosphere. Carbon monoxide rotational spectra are probably important in cooling the high atmospheres of Mars and Venus.

Nitric oxide has a vibration–rotation band at 5.3 μm whose importance could not be assessed until the NO concentration was established. It is, in fact, highly variable; one sample calculation leads to a loss of 0.45 erg cm^{-2} s^{-1}. Prior to 1980, the principal radiative loss for the upper thermosphere of Earth was thought to be a forbidden (by electric-dipole radiation) transition between two of the fine-structure levels, $J = 1 \rightarrow J = 2$, of the ground term of

$O(^3P_{2,1,0})$ (cf. Fig. 6.3). The transition occurs at 63 μm. The level separation (0.02 eV) is comparable to atmospheric thermal energies (0.02 eV = 232°K). Because the radiative lifetime is so long ($1/A = 3.1$ hr) compared with the time between thermal collisions, the levels of the O ground term are in a Boltzmann distribution. Hence the emission rate at 63 μm is

$$\frac{dE(1,2)}{dt} = [\mathrm{O}]\frac{\tilde{\omega}_1 \exp(-E_1/kT)}{\sum_{J=0}^{2} \tilde{\omega}_J \exp(-E_J/kT)} A(1,2)E_1 \qquad (1.7.18)$$

where E_J is the energy of the Jth level above ground ($J = 2$). The cooling effect of this radiation is important, however, only above the level where the transition ceases to be optically thick and this consideration limits the cooling to the F region (see Problem 1.7). The $J = 0 \rightarrow J = 1$ transition at 147 μm also occurs, but is less important.

1.7.4 Conductive Flow of Heat and Location of the Mesopause

With a positive temperature slope, preventing convection, and a not very effective exchange of heat by radiation, the primary energy transfer in the lower thermosphere is by conduction. The instantaneous rate of heating is

$$\rho \frac{\partial}{\partial t}(C_p T) = \frac{\partial}{\partial z}\left(K \frac{\partial T}{\partial z}\right) + \sum_i \pi \mathscr{F}_i \varepsilon_i \alpha_i N(z) e^{-\tau_i(z)/\mu} - \mathscr{R}(z) \qquad (1.7.19)$$

We here divide the solar flux into a number of spectral intervals $\pi\mathscr{F}_i$, chosen so that the absorption coefficient has little variation within each one. Thus $\pi\mathscr{F}_i$ is the solar energy flux (erg/cm^2 sec) within each interval, ε_i is the fraction of absorbed solar energy that appears locally as heat, and $\tau_i(z)$ is the vertical optical thickness in the ultraviolet intervals. With α_i the mean absorption cross section (cm^2/molecule), we have $d\tau_i = -N(z)\alpha_i\, dz$. Also $K(T)$ is the thermal conductivity (erg/cm sec°K) and $\mathscr{R}(z)$ is the radiant heat loss (erg/cm^3 sec).

In a steady state, averaged over a day, this equation integrates to

$$K\frac{dT}{dz} = \tfrac{1}{2}\sum_i \pi \mathscr{F}_i \varepsilon_i \langle\mu\rangle \left[1 - \exp\left(\frac{-\tau_i}{\langle\mu\rangle}\right)\right] - \int_z^\infty \mathscr{R}(z)\, dz \qquad (1.7.20)$$

which is equivalent to the downward conductive heat flux. The use of an average solar zenith angle, $\cos^{-1}\langle\mu\rangle$, is an approximation (as is the factor $\frac{1}{2}$ for nighttime). The flux should actually be integrated through the day with $\mu = \mu(t)$.

It is clear that at high altitude the right side vanishes and $T \rightarrow T_{ex}$, the exospheric temperature. At other heights z, the gradient must be large enough

to sustain a downward flow of heat equivalent to the total ultraviolet energy absorbed above z less the infrared loss.

Figure 1.13 shows where the energy is absorbed in the two intervals 80–1026 Å and the Schumann–Runge region, $\lambda < 1750$ Å. The ionization energy varies with solar activity, but is the order of 2 erg/cm^2 sec. The Schumann–Runge flux is the order of 15 erg/cm^2 sec. The radiant loss from 63 μm radiation of O is probably only a few tenths of an erg/cm^2 sec, although that could be important above 150 km. The high altitudes are well insulated from the mesosphere by the thick thermosphere through which heat must flow to escape. Consequently, small changes in the heat absorbed or emitted can have a big impact on the local temperature.

$K(T)$ can be represented by the expression

$$K(T) = AT^s \qquad (1.7.21)$$

where values of the empirical constants A and s are given in Table 1.2. The net heat flux deposited above 120 km, where $T \approx 325$°K, is therefore

$$K(T)\frac{dT}{dz} = \tfrac{1}{2}\pi\mathscr{F}\varepsilon\langle\mu\rangle \gtrsim 0.4 \text{ erg/cm}^2 \text{ sec} \qquad (1.7.22)$$

in order to support a gradient of at least 15°K/km, higher gradients occurring with high solar activity. Thus the ionization energy alone deposited above 120 km can probably account for the gradient with, say, $\langle\mu\rangle = \frac{1}{2}$ and $\varepsilon = 0.8$.

The gradient at 90 km is only some 10°K/km, but a glance at Fig. 1.13 shows that the overhead heat input has increased manyfold. Even with some differences in efficiency, the conclusion is clear that radiative loss is important in the 100 km region. The location of the mesopause is given by the altitude at which the entire thermospheric flux has been radiated away by CO_2, at 15 μm.

With CO_2 in vibrational relaxation, Eqs. (1.6.18) and (1.6.19) give the mesopause condition as

$$f(\mathrm{CO_2})\eta(1,0)h\nu \int_{z_0}^{\infty} \mathrm{N}^2(z) e^{-h\nu/kT}\, dz = \tfrac{1}{2}\pi\mathscr{F}\varepsilon\langle\mu\rangle \qquad (1.7.23)$$

TABLE 1.2 *Constants in the Expression for Thermal Conductivity*[a]

	Gas					
	N_2, O_2	O	CO_2	H	H_2	H_2
Range (°K)					>150	<150
A	36	54	0.82	235	252	68.6
s	0.75	0.75	1.28	0.75	0.751	1.0

[a] Equation (1.7.21). The units of A are erg cm (cm^2 sec °K)$^{-1}$.

where $f(CO_2)$ is the mixing ratio of CO_2 (3×10^{-4}) and $\eta(1,0) = 2.5 \times 10^{-15}$ cm^3/sec. The conductive flux on the right is about 3.4 erg/cm^2 sec. Evaluating the integral in the isothermal approximation (1.1.4) at $T_0 = 175$°K (the solution is not sensitive to T_0) we find

$$N(z_0) = 1.3 \times 10^{14}\ \text{cm}^{-3} \tag{1.7.24}$$

which occurs around 85 km.

The heat equation (1.7.22) can be solved analytically for a simplified but moderately realistic situation (see Problem 1.11). The thermosphere is represented as a conducting slab obeying (1.7.21) with the heat source concentrated at the top (the thermopause) and the sink at the bottom (the mesopause, at T_0). The vertical coordinate is transformed to pressure by the hydrostatic equation (1.1.3):

$$\ln p = \ln p_0 - \int_{z_0}^{z} \frac{dz}{H} \tag{1.7.25}$$

Substitution of (1.7.22), with its right-hand side set equal to Q, followed by integration, yields

$$T^s = T_0^s + (skQ/AMg)\ln(p_0/p) \tag{1.7.26}$$

Because pressure is proportional to integrated density [Eq. (1.1.6)], the ratio of pressures is the same as the ratio of optical depths. To find the thermopause temperature T_1, we assume that this level is at a slant optical depth of unity; thus, $p_0/p_1 = \tau_0/\langle\mu\rangle$, where τ_0 is the optical depth at the mesopause for the softest ultraviolet radiation ($\sim$200–1000 Å).

A full numerical solution, including heat sources and sinks within the thermosphere, is easy using a similar technique. However, it still includes many uncertainties in the solar flux, the heating efficiency, and the mesopause conditions; in reality, the approximate analytic solution may be all that is justified.

1.8 Atmospheric Structure of Venus, Mars, and Mercury

1.8.1 Venus

The high temperature of the surface, 733°K at 92 bars, was first deduced from its emission in the microwave radio spectrum, to which the atmosphere is nearly transparent. Although only a few percent of the solar flux reaches the ground, the high temperature is due to a greenhouse effect. The gas is nearly all CO_2, with about 3% N_2 (see Table 4.1).

The first measurements of the temperature profile were made by radio occultation (cf. Section 5.2.2) of Mariner 5 and by *in-situ* sensing on the

Venera 8 probe. Both kinds of measurement have since been repeated; the data in Fig. 1.14 are from the Pioneer Venus probes and orbiter. The lapse rate below 60 km is close to the adiabatic value but is actually less on average by about 1°K/km. There are thin layers typically around 20 and 50 km that are significantly unstable. Horizontally, this whole region is globally uniform to within about 5°K. Both this uniformity and the vertical structure represent the effects of dynamical activity.

The 50–65 km region is occupied by a dense, nearly uniform, cloud with an optical depth of about 20. Thin haze extends to much higher altitudes, 80–90 km. The principal cloud material is concentrated H_2SO_4, with approximately one H_2O molecule per H_2SO_4 molecule. The yellow color is most commonly attributed to sulfur, and there is evidence of a third component,

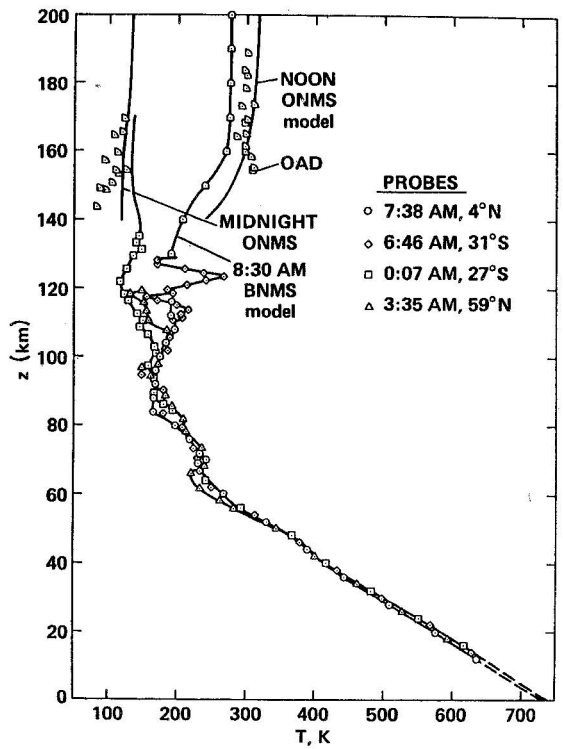

Fig. 1.14 Temperature profiles of the Venus atmosphere from the surface to 200 km, compiled by Seiff from Pioneer Venus observations. The acronyms refer to various experiments: B, probe bus; O, orbiter; NMS, neutral mass spectrometer; and AD, atmospheric drag. [After Hunten *et al.* (1983).]

also solid, near the cloud base. The first identification of sulfuric acid was from the refractive index (1.45) and near-infrared reflectivity (cf. Section 5.2.2), and several probe experiments have provided ample confirmation.

Winds have been measured at the cloud top by the tracking of features, and down to the surface by the tracking of probes. The flow is almost exactly zonal and retrograde (east to west). Although the direction is the same as for Venus' rotation, the speeds at the cloud top are much greater; the period is about 4 days rather than 243 days (sidereal). This speed of 100 m/sec decreases roughly linearly with height, reaching unmeasurably small values (less than 10–20 cm/sec) at around 5–10 km. These speeds refer to low latitudes; further north and south, the speeds diminish somewhat more slowly than they would for a solid shell. Above 65 km there is no direct information, but there are indications of a maximum speed of 120 m/sec followed by a decline.

Figure 1.14 shows a nearly monotonic decline of temperature from 65 to 100 km; there is no signature of a stratosphere, and we shall refer to the entire region as the mesosphere. As in the troposphere, any diurnal variation is very small.

On the day side the temperature begins to rise above 100 km, reaching an asymptotic value of 300°K at about 170 km. This thermosphere is therefore not nearly as well developed as the Earth's (compare Figs. 1.14 and 1.1). The night sides show an even more striking difference. The diurnal variation of exospheric temperature on Earth is around 200°K, or 20%. On Venus it is again 200°K, but this is now a factor of 3. Another view of this variation is shown in Fig. 1.15, which covers $2\frac{1}{2}$ Venus days with daily measurements based on the scale height of atomic oxygen: $T = MgH/k$ with $M = 16$ amu (cf. Eq. 1.1.3). The term "thermosphere" (heat-sphere) becomes rather

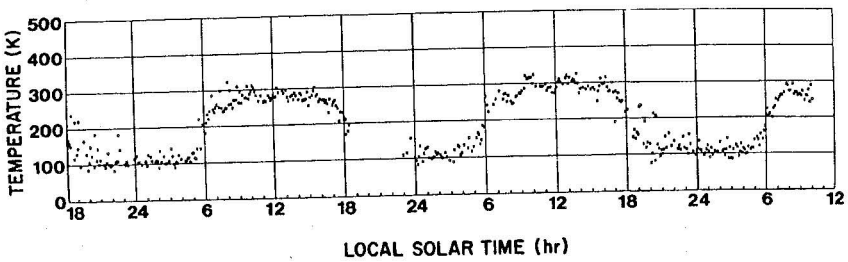

Fig. 1.15 Diurnal variation of the exospheric temperature derived from constituent scale heights measured by the Pioneer Venus orbiter mass spectrometer. One point is shown for each Earth day; the time covered is about $2\frac{1}{2}$ Venus days. [After HUNTEN *et al.* (1983).]

strained on the night side, and "cryosphere" is in common use. The same word is conventionally applied to regions of ice and snow on the Earth, but confusion is unlikely

The composition of the upper thermosphere and lower exosphere are shown in Fig. 1.16. The cutoff at 150 km represents the lower altitude limit of the Pioneer Venus Orbiter and is already well above the homopause. Dashed and solid curves represent mean conditions near noon and midnight, where O becomes the dominant constituent at 157 and 140 km. The vastly different scale heights correspond to the different temperatures. Figure 1.17 shows the H density at 165 km as a function of hour angle (midnight at 0 and 24, noon at 12). For this gas, the effect of differing scale heights is small, and the maximum densities are on the night side. However, the peak is around 4 a.m., not midnight. A similar offset bulge is seen in airglow at 1980 Å (the 0-1 band of the NO δ system) which is excited in recombination of N and O atoms.

Data for the lower thermosphere are very limited. As Fig. 1.14 indicates, some temperature profiles were obtained by analysis of the drag on the Pioneer Venus probes. In addition, a mass spectrometer on the probe carrier (or bus) measured helium and CO_2 down to 130 km, which is below the homopause. Along with some airglow data, these results can be used to constrain an aeronomical model and give the results shown in Fig. 1.18 (also, cf. Section 2.3.5).

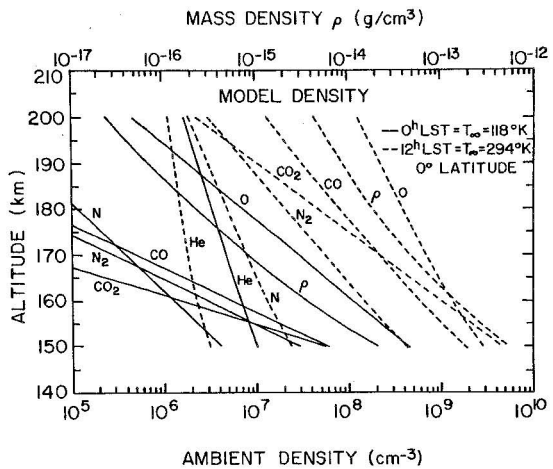

Fig. 1.16 Model densities for the thermosphere derived by a global fit to data of the Pioneer Venus orbiter mass spectrometer. Recalibration suggests that all densities should be multiplied by 1.63. [After NIEMANN *et al.* (1980).]

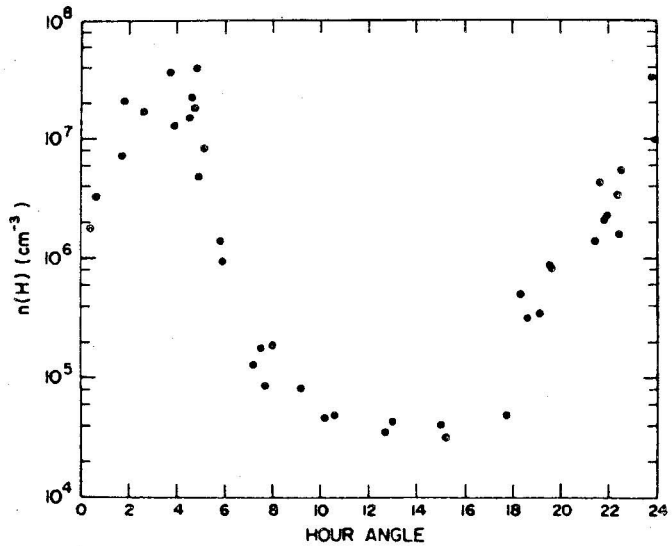

Fig. 1.17 Diurnal variation of H on Venus near 165 km derived from other ions and the O density according to (5.1.42b). [After BRINTON *et al.* (1980).]

1.8.2 Venus' Thermosphere and Cryosphere

The large diurnal density ratio evident in Fig. 1.17 is accompanied by an even larger pressure ratio that is proportional to both density and temperature ratios [Eq. (1.1.2)]. Strong day-to-night winds would therefore be expected and were, in fact, predicted before there were any data for the night side. The pressure differences are, however, much greater than predicted. There are no wind measurements at thermospheric heights, but the nightside maximum of H (Fig. 1.17) and the NO airglow maximum give strong indications that the expected winds do exist. The displacement of both maxima away from midnight indicates that the flow is unsymmetrical and suggests that there is a superposed rotation. A sketch of the proposed flow field is shown in Fig. 1.19. The direction of the rotation is the same as that of the planet and the cloud tops. The speed can be estimated by the following argument. The rotation speed must be around one-half the day–night wind speed to cause the observed displacement of the maxima. If the wind speed is 100–200 m/sec (approaching the speed of sound), the rotation would be 50–100 m/sec. The corresponding period is around 6 days.

The circulation must be closed by a night-to-day flow, which is expected to be in the upper mesosphere around 90 km. As the major gases descend to

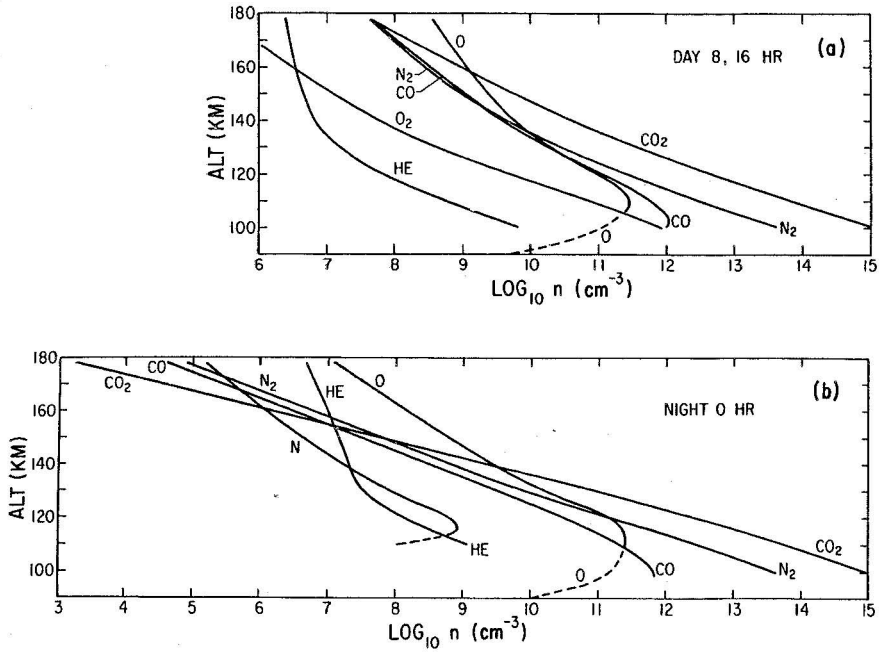

Fig. 1.18 Densities for the Venus thermosphere on the day and night sides obtained from one-dimensional models based on Pioneer Venus and airglow data. [After MASSIE *et al.* (1983).]

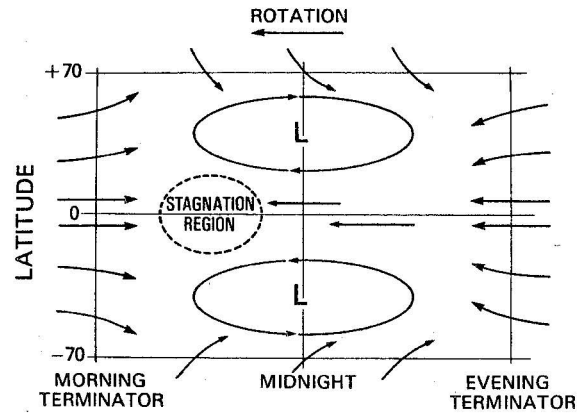

Fig. 1.19 Schematic horizontal flow field for the nightside Venus thermosphere. [After NIEMANN *et al.* (1980).]

complete this circulation, they leave behind the lighter ones (H, He, N, O) to form the observed bulges. Horizontal flow in a diffusively separated region has the unusual property that the amount of each gas carried along is proportional to its scale height as well as its number density. This effect is called *wind-induced diffusion* or a *Johnson pump mechanism.*

The heat balance of Venus' thermosphere offers two unsolved problems: the existence of the nightside cryosphere and the low temperature even on the day side. Substitution of the appropriate parameters into (1.7.26) gives a thermospause temperature of 414°K (Problem 1.12). Even though the heating efficiency is taken to have the remarkably low value of 0.1, this temperature does not agree with the observed global mean of 213°K or even the dayside value of 300°K. Heat transport may be dominated by the global circulation discussed above.

The cryosphere is totally out of the framework of Section 1.7.4, which assumes downward conduction as the principal heat sink. With the observed negative temperature gradient, conduction becomes a source, not a sink. Additional heat is brought in by the winds from the day side. It has been suggested that these winds may be slower than the 100–200 m/sec given by straightforward theory. The flow could become turbulent, which in itself slows down the net motion and also may generate a turbulent viscosity. Another, not entirely distinct, possibility is forced vertical mixing, which in the limit could give a temperature gradient approaching the adiabat. The only heat sink seems to be thermal radiation, principally in the 15 μm bands of CO_2 (Section 1.6), even though it is necessarily very weak at temperatures as low as 125°K.

1.8.3 Mars

Like Venus, Mars has a CO_2 atmosphere with a few percent N_2 (Table 4.1). The surface pressure is, however, far lower, around 6 mbar at a mean level. Temperatures can be measured up to 25 km by radio occultation, and two profiles up to 200 km were obtained during the Viking entries.

Figure 1.20 shows a shaded area that includes the temperature measurements with height at various positions and times of day for dusty conditions. The temperature gradient is not even close to the predicted adiabatic lapse rate of 5°K/km for a clear CO_2 atmosphere in radiative-convective equilibrium. The actual temperature profile is due mainly to absorption of direct solar radiation by dust in the atmosphere. The effect is important even when the atmosphere appears to be clear; although the lapse rate is more nearly adiabatic for clear conditions, it is seldom steeper than 3°K/km. Models of the large-scale circulation (Section 2.5) also give a smaller lapse rate than does convection.

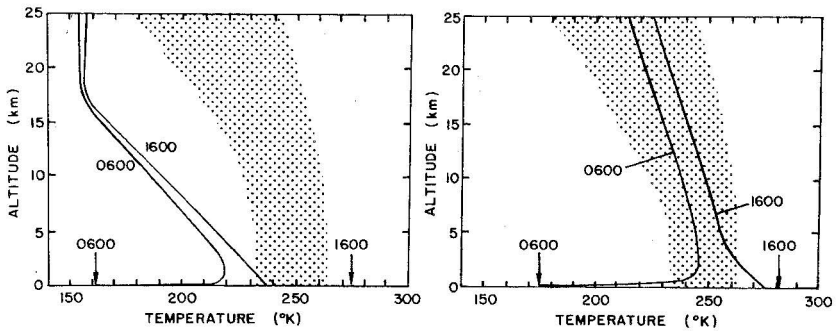

Fig. 1.20 Temperature profiles for Mars showing the effect of direct solar heating due to dust absorption. The shaded areas show the region of Mariner 6 and 7 observations. The curves at the left are calculated for a clear CO_2 atmosphere and at the right for one containing dust. [Calculations are due to GIERASCH and GOODY (1972).]

Because the surface pressure is so low, the greenhouse effect is weak, and the surface temperatures undergo large diurnal variations during the Martian day of 24.660 hr (Fig. 1.21). The Viking entry results are shown in Fig. 1.22. From 0 to 120 km, a combination of directly sensed data and densities from drag deceleration was used. At greater heights, individual densities were obtained by a mass spectrometer. The atmosphere was much less dusty for these 1976 measurements than for the 1969 results, shown in Fig. 1.20, and

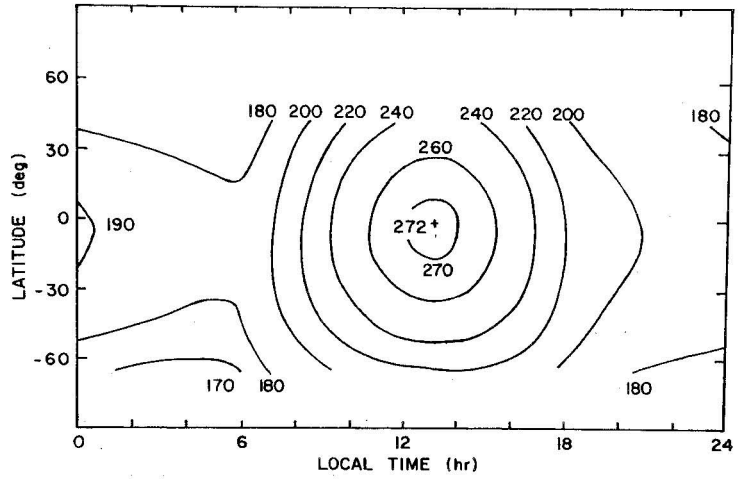

Fig. 1.21 Surface temperatures on Mars, calculated for a clear atmosphere based on Mariner 9 infrared radiometer observations. [Adapted from KIEFFER *et al.* (1973).]

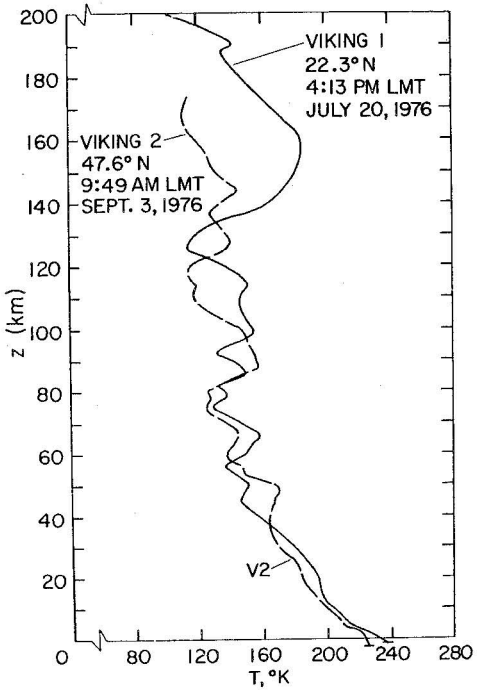

Fig. 1.22 Martian temperature profiles from synthesis of Viking entry data. [After SEIFF and KIRK (1977).]

has a correspondingly larger lapse rate. As for Venus, there is no stratosphere and a very poorly defined mesopause. There is no evidence of a thermosphere in the Viking 2 data; even for Viking 1 the typical temperature is only 160°K.

Water vapor is present in small, highly variable quantities. It can be observed from Earth when the Doppler shift is large enough to move the Martian absorption lines away from the telluric ones (Fig. 4.11). It was also studied in detail by the Viking Orbiters. In the illuminated part of the winter hemisphere the abundance can drop below 1 μm of precipitable water (10^{-4} g cm^{-2}); the largest value seen by Viking was 100 μm near the north polar cap just after it had shrunk to its smallest size. This residual cap was therefore deduced to be water ice. A value around 10 μm is fairly typical.

The atmosphere is always dusty, and dust storms on several scales are frequent. The largest scale covers the whole planet; one of these global storms was in progress in 1969 when Mariners 6 and 7 arrived, and only the tops of four huge volcanoes could be seen. Clouds and hazes of water frost are frequent, and CO_2 itself condenses over the winter pole. These polar caps disappear, except for small remnants, in the summer season. The marked

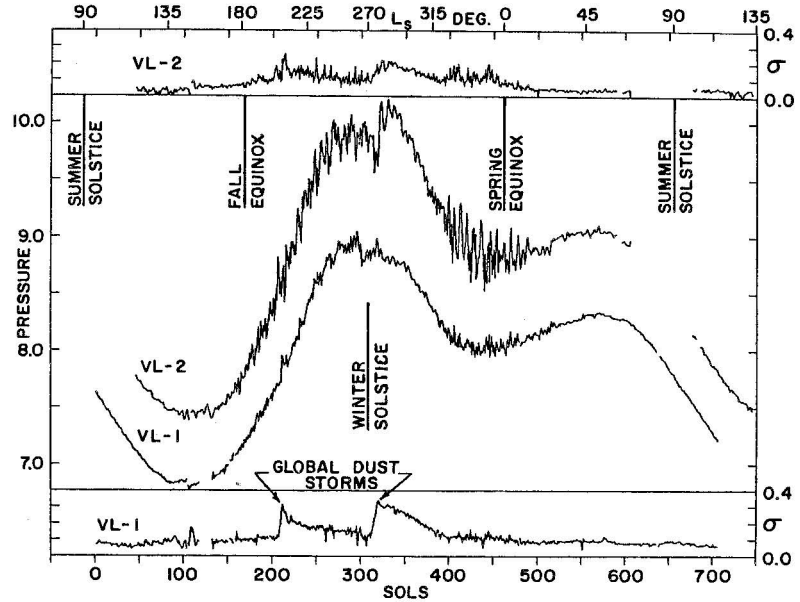

Fig. 1.23 The annual cycles of atmospheric pressure at the two Viking landers. The strips at top and bottom show the standard deviation for each Martian day. [After HESS *et al.* (1980).]

effect on the atmospheric pressure is seen in the data from the Viking landers in Fig. 1.23. Both vehicles were in valleys and, therefore, obtained pressures appreciably greater than the more typical 6 mbar.

Figure 1.23 also shows the effects of Martian weather in the irregular oscillations of pressure about a smooth curve and in the upper and lower data sets which show the variability of pressure within each sol (Martian day). These fluctuations are particularly marked during two global dust storms.

The global circulation is similar to that of the Earth in many ways. Although the latent-heat effects of water are essentially lacking, there is the new feature of migration of 25% of the atmosphere into and out of the polar caps. The enhanced weather activity during late fall and late winter are evident in the pressure data of Lander 2, which was closer to the cap than Lander 1.

1.8.4 Mars' Thermosphere

The composition of the region above 120 km is shown in Fig. 1.24 for Viking 1 conditions with a thermopause temperature of just over 200°K.

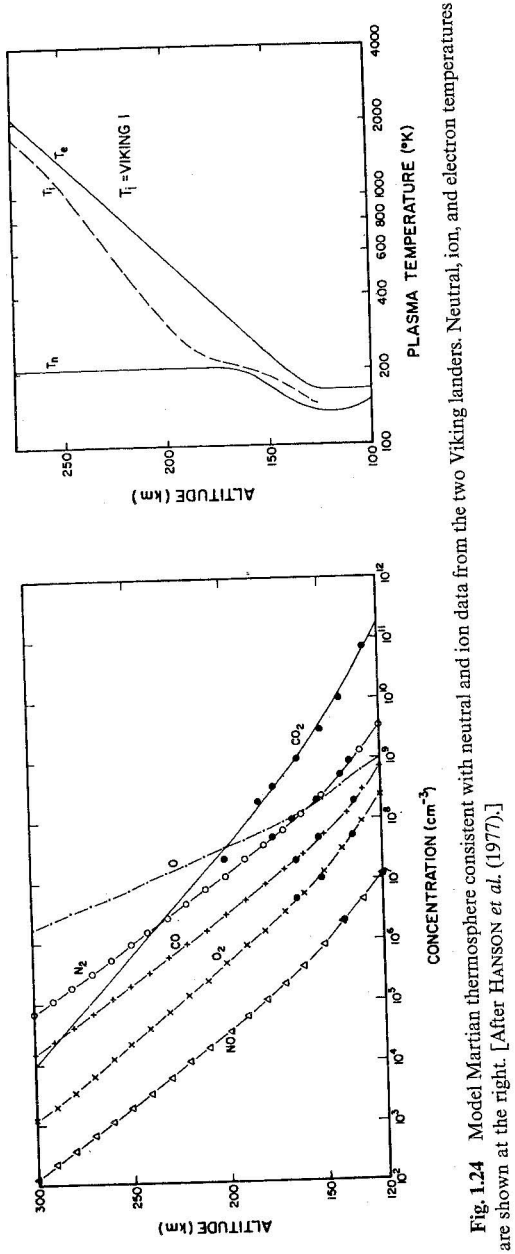

Fig. 1.24 Model Martian thermosphere consistent with neutral and ion data from the two Viking landers. Neutral, ion, and electron temperatures are shown at the right. [After HANSON *et al.* (1977).]

Mass spectrometric data are shown as black dots, and the model as a whole is consistent with ionospheric data. Except for the larger scale heights and the presence of NO, the resemblance to Venus (Figs. 1.16 and 1.17) is close.

However, closer examination shows that Mars is relatively deficient in O and CO. A conventional place to make the comparison is at a CO_2 column density of 4×10^{16} cm^{-2}, which is at unit zenith optical depth for ionizing radiation, and can therefore be loosely called the *ionospheric peak*. The height happens to be near 140 km for the day sides of both planets. According to Fig. 1.16, the O and CO mixing ratios on Venus are 13% and 9%, respectively; Fig. 1.24 shows 1.5% and 0.6%, respectively. The ratios are both near 10, most of which is explained by the ratio of solar fluxes, 4.5, responsible for the photolysis of CO_2. The remaining factor of 2 must reflect different sink strengths, which are almost entirely due to downward transport of the gases out of the region where they are produced. This transport must be about twice as effective on Mars as on Venus.

We now return to the thermospheric temperature profiles shown in Fig. 1.22. They were observed less than two months apart, and both refer to the day side. The mesopause height, computed as in Section 1.7.4, is about 100 km. Thus, even the Viking 1 profile bears very little resemblance to a terrestrial thermosphere such as shown in Fig. 1.1—anything resembling a mesopause is seen only at 130 km.

The temperature rise across the thermosphere should be nearly the same for Mars and Venus (Problem 1.12). Mars, therefore, seems to violate the model of Section 1.7.4 even more thoroughly than Venus. Further information is available from radio occultation studies with the Viking orbiters and Mariners 4, 6, 7, and 9. These results are collected in Fig. 1.25, along with a representation of solar activity. The measured quantity is the topside scale height of the electron density, shown on the left of the figure proper. A temperature can be obtained only through a model, and the one adopted for the scale on the far left assumes an atmosphere of pure CO_2, with ions of CO_2^+ only. The 1978 point from Viking is 200°K. On both Mars and Venus, O^+ and O_2^+ are important, and a model including them gives a lower temperature for the same observed electron scale height. A representative value from Fig. 1.22 is 150°K or perhaps slightly less. To a first approximation, therefore, the temperature scale in Fig. 1.25 should be multiplied by 0.75. The highest point (1969) becomes 300°K. This is comparable to the Venus temperatures in 1980, also a year of high solar activity. However, Venus conditions since then seem to be much less variable than indicated for Mars.

There are no data at all for the nightside thermosphere; the electron density has never been high enough to detect. The rapid rotation of Mars leaves only 12 hours for cooling, which should be slow at the low

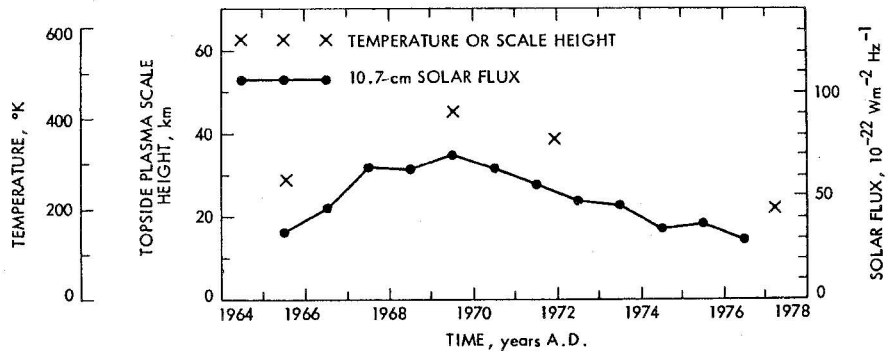

Fig. 1.25 Ionospheric scale heights from Mariner and Viking radio occultations with a solar-flux index for comparison. The temperature scale is valid only for pure CO_2 ions, as discussed in the text: ×, temperature or scale height; ●, 10.7 cm solar flux. [After FJELDBO *et al.* (1977).]

temperatures observed on the day side. This argument suggests that the diurnal variation should be small, but our understanding is too poor for a confident prediction.

1.8.5 Mercury and Moon

These two objects have much in common, but the Moon lacks a planetary magnetic field and has much less atmosphere. The rest of this section will therefore be devoted to Mercury. An upper bound (2×10^{-12} bar) to the total pressure follows from the absence of detectable absorption at the limb below 950 Å The corresponding bound on the number density is 4×10^7 cm^{-3}. However, resonance scattering by H and He at 1216 and 584 Å gives densities of 8 and 4500 cm^{-3} on the day side. There is much more helium on the night side, as inferred from its twilight effects. The larger density, at the much lower temperature, is required to balance the fluxes across the terminator. This problem is treated in Section 7.2.5.

Ground-based observations have found the Na Fraunhofer D lines in emission. The mechanism is almost certainly resonant scattering of sunlight by sodium vapor in Mercury's atmosphere. The total column abundance is estimated at 8.1×10^{11} atom/cm^2, which corresponds to a surface density at the subsolar point of about 1.5×10^5 atom/cm^3. Thus, sodium is at least a major constituent of Mercury.

Later Earth-based spectra also showed the potassium resonance lines at 7699 A. The column abundance ratio is approximately [Na]/[K] = 100.

1.9 Atmospheric Structure in the Outer Solar System

The four Jovian planets, Jupiter, Saturn, Uranus, and Neptune, have extremely deep atmospheres of H_2 with roughly 10% (by number) He. They contain (or are expected to contain at deeper levels) the hydrides of the abundant elements C, N, and O—that is, methane (CH_4), ammonia (NH_3), and water vapor (H_2O). Their mixing ratios tend to be around 0.1% on Jupiter and Saturn and may rise to 1% or even more on Uranus and Neptune. All but methane are nearly absent above levels of a few tenths of a bar, and this gas is nearly transparent above 1400 Å. Ultraviolet solar radiation is therefore much more prevalent in the stratospheres and mesospheres than on the terrestrial planets (although the incident fluxes are much smaller, 0.1–4% of the values on Earth).

Titan, the large satellite of Saturn, has a very substantial atmosphere of N_2 with a few percent of methane. In the Jovian system, Io has a thin SO_2 atmosphere, and the other three Galilean satellites (Europa, Ganymede, and Callisto) have exposed ice and, therefore, undoubtedly at least some water vapor. Methane is seen on Triton and Pluto.

The data shown above for Venus and Mars are heavily based on direct measurements within the atmospheres. No such data are available in the outer solar system. Remote-sensing data from spacecraft are available for the Jupiter, Satern, and Uranus systems. Neptune will be visited in 1989. For Pluto, all the data come from Earth and Earth orbit. (See Appendix IV.)

1.9.1 Jupiter

The temperature profile in Fig. 1.26 was obtained by inversion of infrared radiances, combined with radio-occultation data to fix the helium abundance (Section 4.4). The evidence for the three cloud layers is more or less indirect; their composition is based almost entirely on expected abundances combined with vapor pressures. The presence of at least two separate layers is supported by imaging, inferences from spectroscopy, and infrared radiometry, and there is some evidence for three layers.

If Jupiter has a surface, it may be at a depth of tens of thousands of kilometers and a pressure of a magabar. Heights must therefore be measured from a totally arbitrary level, and there is no unanimity on which level to choose. The primary scale in Fig. 1.26 is the logarithm of pressure, plotted downward, and this practice is common. The height reference is the estimated H_2O cloud base; other choices are 1 bar, the ammonia cloud top, 1 mbar (as in Fig. 1.27), and 1 μbar.

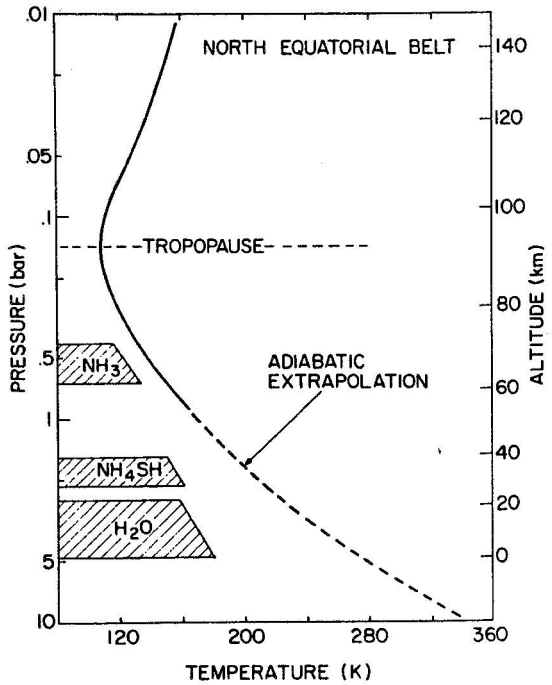

Fig. 1.26 Jovian temperatures and schematic cloud structure, based primarily on Voyager infrared data. The height scale starts at the cloud base, approximately 5 bars. [After KUNDE *et al.* (1982).]

Figure 1.26 shows the tropopause at about 140 mbar and 105°K. The radiative-convective boundary is probably near 400 mbar, the ammonia cloud top. Jupiter's internal heat flux (Table 1.3) is sufficient to ensure convective transport at depths below a few bars, to which solar radiation is expected to penetrate. A very slightly superadiabatic lapse rate is therefore expected at all depths below 400–600 mbar. In practice, the difference is so small that the adiabatic profile can be used. This lapse rate is 1.9°K/km to temperatures of a few hundred degrees; at deeper levels the specific heats begin to rise and real-gas effects become appreciable.

The internal heat flux is obtained from the difference between the observed effective temperature T_{eff}, 125°K, and the solar-equilibrium temperature, 106°K, obtained from (1.2.46). It is believed that Jupiter is still in a late phase of its *Helmholtz contraction* from an initial state of much lower density and is converting the released gravitational energy into heat.

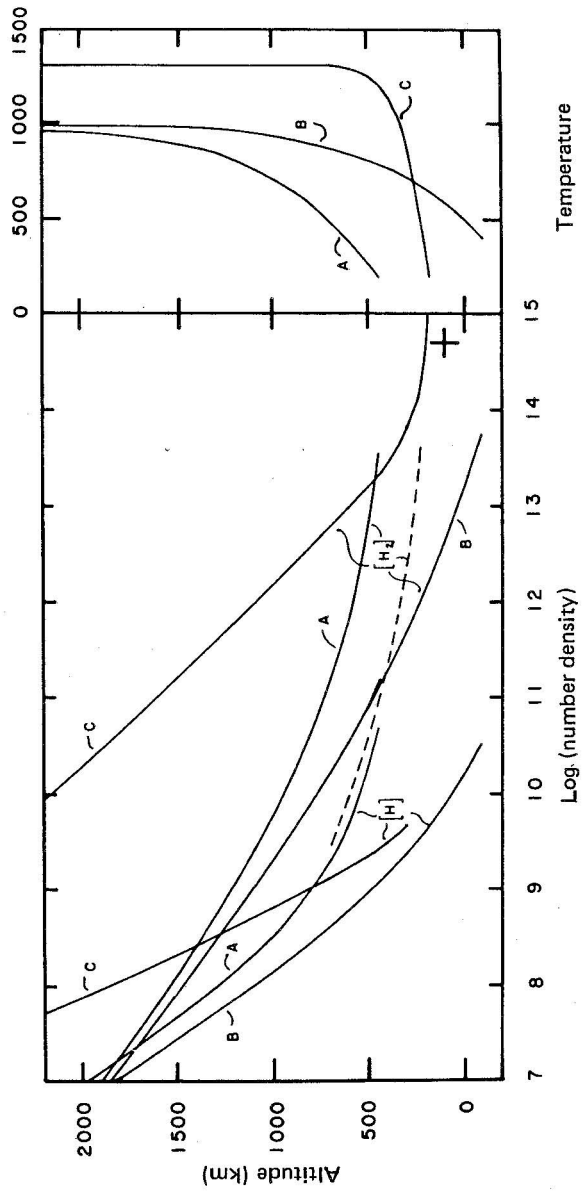

Fig. 1.27 Jovian thermosphere, based on Voyager ultraviolet occultation data; the + point is from earth-based stellar occultations. Curves *A* and *B* fit the above data; curve *C* would be required to fit ionospheric data with no vertical transport other than diffusion. Helium is omitted because the observations were not sensitive to it. [After MCCONNELL *et al.* (1982).]

TABLE 1.3 *Characteristics of the Jovian Planets*

	Jupiter	Saturn	Uranus	Neptune
Mean density (g/cm^3)	1.34	0.70	1.58	2.30
Effective temperature (°K)	124.4	95.0	58	55.5
Equilibrium temperature (°K)	109.5	82.3	57	46
Total flux/solar heat	1.668	1.78	<1.3	1.1
Internal flux (erg cm^{-2} sec^{-1})	5444	2000	<180	285
Adiabatic lapse rate (°K/km)	1.9	0.84	0.85	0.86
Tropopause temperature (°K)	105	85	54	52
Tropopause pressure (mbar)	140	80	100	200
Exospheric temperature (°K)	700–1000	420	700	—

Figure 1.26 shows a well-developed stratosphere, whose full extent is not included. Radio-occultation data extend somewhat higher and, along with other data, suggest a stratopause at about 1 mbar and 160–170°K overlain by an isothermal mesosphere. There are two principal heat sources, both from solar radiation: the 3.3 μm band (ν_3 fundamental) of methane and absorption in the ultraviolet and blue, which is attributed to a dust or smog of photochemical origin and greatly reduces the planetary albedo below that of the known atmospheric gases alone. Similar smogs are observed on Titan and Saturn; they are undoubtedly generated in the photochemistry of methane.

Cooling of the stratosphere and mesosphere is dominated by the 7.7 μm (ν_4 fundamental) of methane and the 12.2 μm (ν_9 band) of ethane (C_2H_6). Although this latter molecule, which is of photochemical origin, is scarce, its band has a much better overlap with the Planck function than the methane band, and it therefore plays an important role. In the upper mesosphere, acetylene (C_2H_2) is expected to become more and more abundant and exceed the ethane in the mesopause region. Acetylene has its ν_5 band at a still longer wavelength, 13.7 μm, and probably controls the level at which all the heat from the thermosphere can be radiated (Section 1.6.2). These abundance estimates are entirely theoretical and very uncertain, and the mesopause level is therefore equally uncertain.

Pioneers 10 and 11, as well as Voyagers 1 and 2, measured the topside ionosphere by radio occultation (Section 5.3.3). If the scale height can be interpreted in terms of a proton–electron plasma, the temperatures found are 750–1000°K. It is expected that this plasma temperature is not significantly greater than the gas temperature. A serious observational difficulty is exhibited below the 1000-km level of Fig. 5.12. This part of the ionosphere is highly stratified, rendering analysis of the occultation data very difficult and the results uncertain. The reason is multipath propagation: more than one ray can reach the observer at a given instant. This difficulty is so severe that

the corresponding Voyager results have not been published, more than five years after the first encounter with Jupiter.

An important advance made by the Voyagers was to obtain solar and stellar occultations (properly called eclipses) in the ultraviolet region from 580 to 1600 Å, which includes the ionization continuum of all gases except helium, as well as bands and other continua at the longer wavelengths. Densities of H and H_2 obtained in this way are shown in Fig. 1.27 (curves *A* and *B*). The differences between these two sets of curves reflect the uncertainties of the analysis. The "plus" symbol in the lower right corner was obtained from Earth-based stellar occultation. Helium is present, but is not observable in the wavelength region used. Curves *C* are the densities required to explain the ionospheric densities by standard theory. It is clear that this theory does not include some important effect or effects, probably upward transport of plasma by winds or external electric fields. Nevertheless, as the right-hand panel of Fig. 1.27 shows, the exospheric temperature is still found to be of order 1000°K.

Application of (1.7.26) gives a predicted temperature rise across the thermosphere of about 15°K (Problem 1.13). Clearly a much stronger source of heat than solar ionizing radiation must be present. Suggested sources are dissipation of gravity waves generated in the troposphere, or soft electrons, either precipitating from outside the atmosphere or accelerated *in situ* by electric fields. They must be soft (that is, very easily absorbed) so that their energy will be dissipated at high altitudes; this energy could be a few electron volts up to a few tens of electron volts. Other phenomena (intense day airglow; high-latitude auroras) also suggest the presence of nonthermal electrons, some of which must have energies greater than the 12 eV photons that are observed. If the heat is deposited at the same height as solar ionizing energy, the flux required is 0.25–0.5 erg cm^{-2} sec^{-1} (cf. Problem 1.13).

1.9.2 Saturn, Uranus, and Neptune

Representative temperature profiles for Saturn are shown in Fig. 1.28. The tropopause temperature is around 85°K at the 80 mbar level. Cloud layers are expected at the same temperatures shown for Jupiter in Fig. 1.26. The ammonia layer , at 150°K, would therefore be somewhat deeper than 1 bar. The base of the H_2O cloud (280°K) is at 11 bars, if the lapse rate is adiabatic as expected. The internal heat flux is about one-third of Jupiter's and therefore a similar fraction of the absorbed solar energy (Table 1.3). However, models of Saturn's Helmholtz contraction do not provide nearly this amount of energy. Instead, it is believed that Saturn is in the process of differentiating: at great depths, helium becomes insoluble in hydrogen, forming droplets that

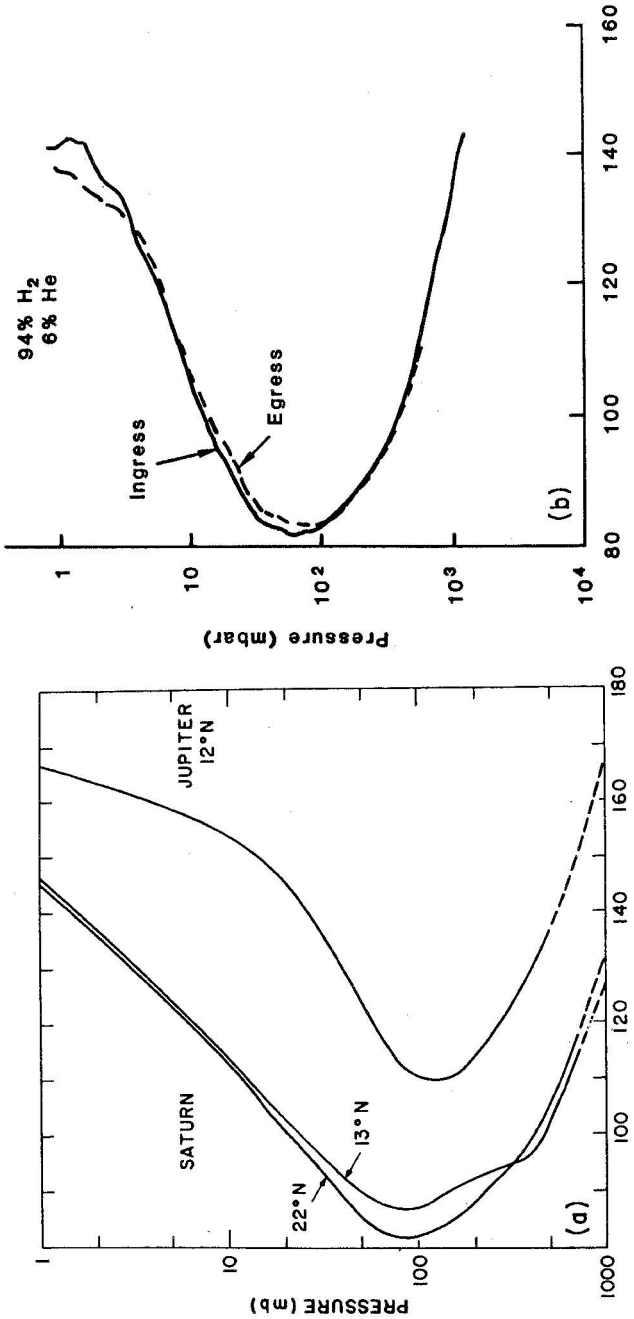

Fig. 1.28 Saturn temperature profiles obtained from (a) infrared and (b) radio-occultation data. [After HANEL *et al.* (1981) and TYLER *et al.* (1982).]

sink and release gravitational energy. Jupiter's interior is too hot for this to happen. Considerable support for the presence of differentiation is given by Saturn's helium abundance, which is considerably less than that of Jupiter (Table 4.1)

A stratospheric temperature rise is evident in Fig. 1.28, with a suggestion in the radio data of a stratopause near 1 mbar. There are no stellar occultation data to give a guide to mesopause conditions, but it appears that the mesospheric temperature could be around 150°K.

Data for the thermosphere and exosphere are shown in Fig. 1.29; as for Fig. 1.27, helium is omitted because the ultraviolet occultation experiment

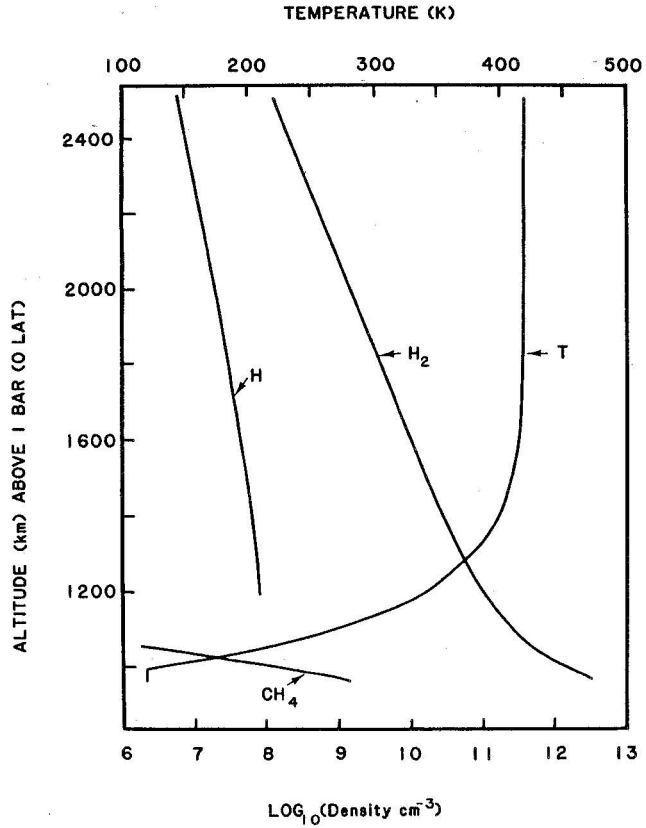

Fig. 1.29 Saturn's thermosphere from ultraviolet occultation. As in Fig. 1.27, the experiment was insensitive to helium. [After SMITH *et al.* (1983).]

could not observe it. Just as for Jupiter, the exospheric temperature is far higher than expected for solar heating alone, and all the remarks about this area made for Jupiter apply equally well to Saturn and Uranus.

Uranus and Neptune have considerably larger mean densities than Jupiter and Saturn (Table 1.3). Moreover, they have less gravitational compression, and must therefore contain much less hydrogen and helium in proportion to the heavier ice- and rock-forming elements. Methane abundances are much greater (1% or more); ammonia and water vapor are not observable at the low temperatures of these atmospheres.

Temperature profiles are shown in Fig. 1.30. The solid and dashed curves are obtained by inversion of Earth-based infrared data, which have almost no information content for pressures below 1–10 mbar. In the mesospheres, the dotted curves represent results from stellar occultations. Usable events are much more common for Uranus and Neptune than for brighter planets, because much fainter stars can be observed. At the very cold temperatures reached in these atmospheres, condensation of methane becomes likely. This effect is responsible for the differences among the various curves of Fig. 1.30 in the 70–100°K (1–3-bar) region, which pertain to mixing ratios of 0.2, 2, and 4‰, reading downward. These values refer to the deeper atmospheres and are reduced at the higher levels by cloud formation; the clouds appear between the bends in the curve. H_2O clouds could form below the 100-bar level and might extend as deep as 500 bars if the abundance is several percent. Clouds have been photographed on Neptune but not on Uranus; Neptune also shows photometric variations that are absent on Uranus.

As Table 1.3 indicates, Neptune has a detectable internal heat flux, while Uranus does not. It is therefore conceivable that the lapse rate on Uranus becomes subadiabatic for pressures greater than a few bars. It is equally possible that the true heat flow is just below the detection limit.

Both planets have stratospheres, although the lower, near-isothermal part is almost certainly much deeper on Uranus. Both mesospheres seem to be at 140–150°K. The Voyager encounter with Uranus obtained results analogous to Fig. 1.29, but with an exospheric temperature of 700°K. Both the high temperature and the presence of discrete aurora suggest nonsolar heat sources as on Jupiter and Saturn.

All four Jovian planets have nearly the same mesospheric temperature, despite solar and planetary heat sources varying by a factor of 30. The likely explanation lies in the spectral location of the C_2H_6 and C_2H_2 bands discussed in Section 1.9.1. At 150°K, the peak of the Planck function is at 19 μm, and it only barely overlaps the 12.2 μm band of ethane; if the temperature drops, the overlap quickly disappears. Thus, there is a very effective thermostat which can accommodate a wide range of heat inputs.

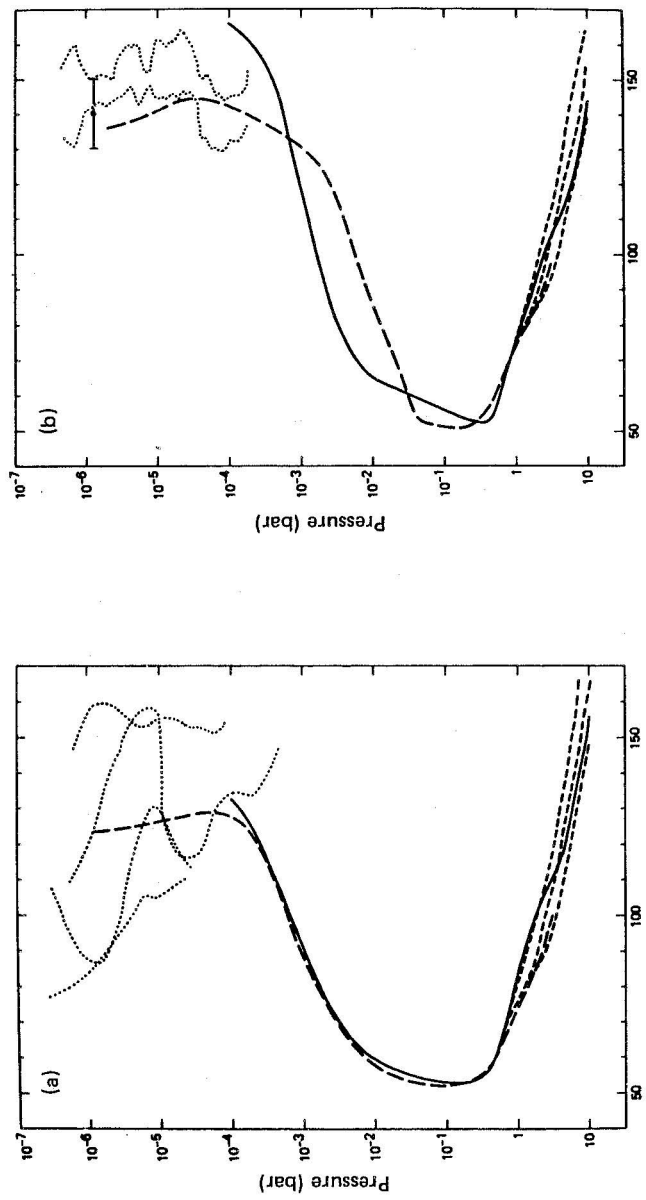

Fig. 1.30 Temperature profiles for (a) Uranus and (b) Neptune from Earth-based infrared and stellar-occultation data. [After Orton and Appleby (1984).]

One unique property of Uranus is its obliquity, which puts the axis almost in the orbital plane. Each hemisphere suffers an intense, 42-year winter which must have profound effects on the stratosphere and mesosphere. At higher pressures, the effects are minimized by a long thermal time constant. Further discussion appears in Section 2.7.

1.9.3 Titan

Titan can be regarded as a terrestrial planet located in the outer solar system. Its mean density suggests roughly equal proportions of rocky and icy material. The atmosphere is mostly N_2, with a surface at 1496 mbar and 94.0°K. Methane absorptions are prominent in the spectrum; the abundance is around 1% in the stratosphere and perhaps 3% near the surface. As these figures imply, a methane cloud layer is suspected to be present, but it is hidden by a thick, pervasive hydrocarbon smog which gives the body a dark orange (really, brown) color. The smog occupies the upper troposphere and middle stratosphere; the cloud, if present, would be in the middle troposphere. A very close pass by Voyager 1 gave excellent infrared data and radio and ultraviolet occultations. Figure 1.31 shows the radio temperature profile, which includes information from the infrared. The tropopause is at 42 km, 128 mbar, 71.4°K. Temperatures around 170°K are reached near 1 mbar. which is probably the stratopause level.

The ultraviolet occultation probed the upper thermosphere and exosphere. The temperatures shown on Fig. 1.32 are very similar to that found at the stratopause. Application of the hydrostatic equation (Problem 1.14) shows

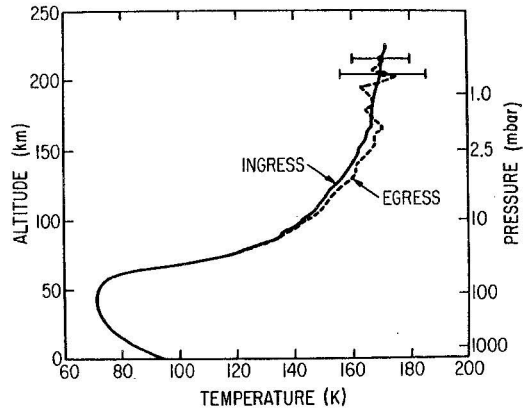

Fig. 1.31 Titan temperatures by radio occultation for a mean mass of 28 amu consistent with infrared results. [After HUNTEN *et al.* (1984).]

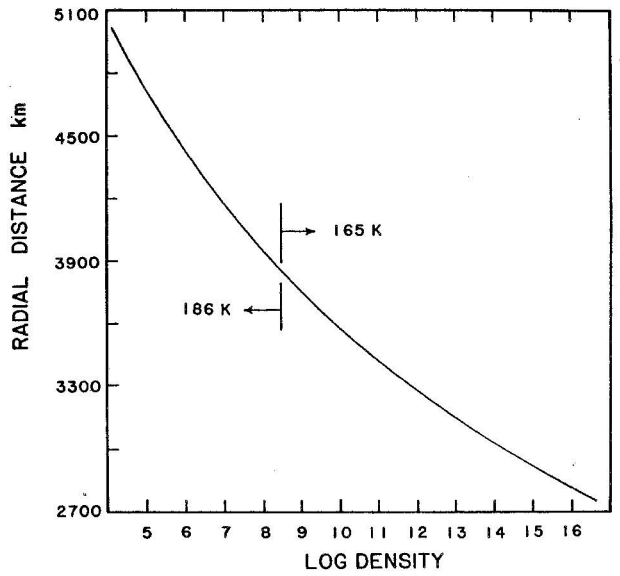

Fig. 1.32 Density (primarily N_2) of Titan's upper atmosphere from Voyager ultraviolet occultation. To compare the heights with Fig. 1.31, subtract 2575 km. [After SMITH *et al.* (1982).]

that the mean temperature between these levels is also similar. This whole region is unlikely to be strictly isothermal, but there is no further information. The density profile in Fig. 1.32 is noticeable curved, even though it is made up of two isothermal sections. The reason is the large variation of gravity with height in this extended atmosphere.

No ionosphere could be detected at a sensitivity level of 2000 cm^{-3}. There are two reasons: the regions probed were near sunset and dawn, and this molecular atmosphere (including methane and other hydrocarbons) provides very fast recombination. Figure 1.32 indicates a temperature step of 21°K at a density of 3×10^8 cm^{-3}, which could perhaps represent a thermosphere, but this density is much less than normal for such a region. In any case, there is no sign of the many hundred degrees of temperature rise seen on Jupiter and Saturn.

Titan's stratosphere is the site of very active hydrocarbon photochemistry (Section 6.4.3). The principal products are the brown smog and ethane, C_2H_6, at the expense of methane, which must be replenished from below. The amount of ethane accumulated over the age of the solar system amounts to several hundred meters of liquid, which presumably exists at the surface along with dissolved methane, nitrogen, and heavier molecules.

1.9.4 Pluto, Triton, and the Galilean Satellites

Pluto's near-infrared spectrum shows several weak but well-defined methane absorptions. The shapes of the bands are more consistent with gas than ice as the absorber; moreover, at the expected temperature (57°K), any ice would have a substantial vapor pressure. If all the absorption is attributed to gas, the abundance is 2700 ± 700 atm-cm, and the surface pressure is 150 μbar. Because of Pluto's large orbital eccentricity, its equilibrium temperature varies appreciably. The measurements quoted here were made in 1980, near the warmest part of the cycle. Considerably lower atmospheric pressures probably occur at other times in Pluto's year.

Triton, the largest satellite of Neptune, also shows methane absorptions, but they are weaker and change appreciably as different sides of Triton face the Earth. The most likely explanation is that at least a major part of the absorption occurs in methane ice, which would be more abundant on one side. It is also possible that there are large topographic differences between the two hemispheres, with more gas over the lower one. In addition, an absorption at 2.16 μm seems to be due to liquid or solid N_2. The vapor pressure at 64°K is 130 mbar, but the actual temperatures may be somewhat lower, especially at high latitudes and at night. The methane partial pressure should be about 10^{-3} times smaller.

Jupiter's Galilean satellites fall into two very different groups: Europa, Ganymede, and Callisto, which exhibit water-ice absorptions, and Io, whose surface is mostly sulfur and SO_2. At Io's subsolar temperature, the vapor pressure of SO_2 is about 10^{-7} bar. This figure is very sensitive to the assumed albedo, and if the SO_2 frost is concentrated in white patches, which would be colder than average, the estimated subsolar pressure drops to 7×10^{-9} bar. Near the terminator the vapor pressure drops to 10^{-11} bar, and on the night side it is less than 10^{-16} bar. In addition, at any one time there are several volcanoes (or geysers) erupting to heights as great as 300 km and probably ejecting large quantities of SO_2 vapor. Whether the actual pressures resemble the vapor pressures is uncertain and is a subject of lively discussion. It has been suggested that the SO_2 frost is located deep in a porous surface, where its temperature excursions would be greatly reduced. Also, if the pressure gradients are large, strong winds will blow away from the subsolar region and will tend to equalize the pressures. Photochemical action on SO_2 must produce at least some O_2 (see Section 6.4.4), which could contribute appreciably to the total pressure, especially on the night side.

Empirical information is indirect and ambiguous enough to permit more than one interpretation. Pioneer 10 observed ionospheres at both limbs by radio occultation, and they can be accounted for by electron bombardment of a 10^{-11} bar atmosphere. The infrared instrument on Voyager 1 detected SO_2 directly, with a surface pressure around 10^{-7} bar, but the line of sight passed through a volcanic plume, which may have been the cause of the absorption. There is no specific reason to apply the same explanation to the Pioneer results, although it cannot be ruled out.

The computed exospheric temperature is 1000°K, consistent with the large extent of the ionosphere. The temperature is high because SO_2 absorbs strongly at much longer wavelengths than the gases found in any of the planets.

Io's orbit is surrounded by a torus containing atoms and ions of O, S, and Na. The ionized part, or plasma, is at a temperature of 50,000°K or 4 eV, and it radiates copiously in the 600–1000 Å region. There can be no doubt that Io is the source of the material, but the mechanisms at work have not been fully identified. There is little doubt that a major one is sputtering, or ejection by impact of energetic positive ions.

No atmospheres have been detected on Europa, Ganymede, or Callisto. An ultraviolet occultation measurement from Voyager 1 set an upper limit for Ganymede of 10^{-11} bar (except for gases that absorb strongly only below 910 Å). All three bodies have water-ice absorptions in their spectra, and should have partial pressures of water vapor in the neighborhood of 10^{-15} bar, which could be increased by sputtering. Photolysis and escape of hydrogen should generate an O_2 atmosphere. The surface pressure is computed to be about 10^{-12} bar (see Section 6.4.4). Alternatively, if the H_2O abundance is 10^{-14} bar or greater, the O_2 is predicted to jump to 10^{-6} bar, which is far above the Voyager limit for Ganymede.

BIBLIOGRAPHICAL NOTES

Section 1.2 Radiative Equilibrium

Atmospheric radiation is the subject of three major books:

GOODY, R. M. (1964), "Atmospheric Radiation," Clarendon Press, Oxford,

is mainly a theoretical account of absorption and heat transfer by atmospheric gases.

KONDRATYEV, K. YA. (1969), "Radiation in the Atmosphere," Academic Press, New York,

deals more with measurements, radiation scattering, global heat balance, and so forth.

ZUEV, V. E. (1974), "Propagation of Visible and Infrared Radiation in the Atmosphere," Wiley, New York,

treats absorption and scattering as well, but the author devotes the final third of his book to the propagation of laser beams.

Radiative transfer is treated extensively in all the above books, but the standard reference is

CHANDRASEKHAR, S. (1950), "Radiative Transfer," Clarendon Press Oxford, (reprinted by Dover, New York, 1960).

The common belief that the heating of a greenhouse is due to the inhibition of convection by

the roof can be traced to experiments described in 1909 by R. W. WOOD. This view has been challenged by

SILVERSTEIN, S. D. (1976), Effect of infrared transparency on the heat transfer through windows: A clarification of the greenhouse effect, Science **193**, 229–231,

who finds that the infrared radiative blanketing is not trivial and the physical analogy with the atmosphere is fairly appropriate after all.

Radiative–convective equilibrium has been the subject of many computer modeling studies. Notable as one of the first thorough attempts along these lines is

MANABE, S. and STRICKLER, R. F. (1964), Thermal equilibrium of the atmosphere with a convective adjustment, *J. Atmos. Sci.* **21**, 361–385.

A thorough review of modeling techniques and results is

RAMANATHAN, V. and COAKLEY, J. A., JR. (1978), Climate modeling through radiative-convective models, *Rev. Geophys. Space Phys.*, **16**, No. 4 (Nov).

Some of the modelling has been concerned with climatic variations due to compositional changes (see Section 7.5).

Section 1.3 Convection in the Troposphere

The breakdown of radiative equilibrium by convective activity was first noted by R. EMDEN in 1913. The surge of theoretical activity following discovery of the stratosphere in 1900 is documented by GOODY (op. cit. Chapter 8).

Section 1.4 Latitude Variations of the Tropopause

The problem of the latitude variation of the tropopause and its dependence on departures from grayness was treated by

GOODY, R. M. (1949), The thermal equilibrium at the tropopause and the temperature of the lower stratosphere, *Proc. Roy. Soc.* **A 197**, 487–505.

Section 1.5 The Stratosphere

The photochemical theory for oxygen in the stratosphere is due to

CHAPMAN, S. (1930a), A theory of upper-atmospheric ozone, *Mem. R. Meteorol. Soc.* **3**, 103–125.

CHAPMAN, S. (1930b), On ozone and atomic oxygen in the upper atmosphere, *Phil. Mag.* **10**, 369–383.

CHAPMAN, S. (1931a), Some phenomena of the upper atmosphere (Bakerian Lecture), *Proc. Roy. Soc.* **A 132**, 353–374.

and to

WULF, O. R. and DEMING, L. S. (1936a), The theoretical calculation of the distribution of photochemically-formed ozone in the atmosphere, *Terr. Magn.* **41**, 299–310.

WULF, O. R. and DEMING, L. S. (1936b), The effect of visible solar radiation on the calculated distribution of atmospheric ozone, *ibid.* pp. 375–378.

WULF, O. R. and DEMING, L. S. (1937), The distribution of atmospheric ozone in equilibrium with solar radiation and the rate of maintenance of the distribution, *ibid.* **42**, 195–202.

The concept that ionizing or dissociating radiation will create "layers" in the atmosphere was first stated quantitatively in

LENARD, P. (1911), Über die Absorption der Nordlichtstrahlen in der Erdatmosphäre, *SitzungsBer. d. Heidelberger Akad. d. Wissenschaften* **12**, 1–9,

and developed more fully for electromagnetic radiation in the first full-length book on radio propagation,

PEDERSON, P. O. (1927), "The Propagation of Radio Waves," Copenhagen, Danmarks Naturvidenskabelige Samfund **A**, Nr. 15a, 15b.

However, it was CHAPMAN who developed the theory to an incredible degree of completeness, including the numerical integration of the equations for a rotating Earth. The "Chapman-layer" papers are

CHAPMAN, S. (1931b), The absorption and dissociative or ionizing effect of monochromatic radiation in an atmosphere on a rotating Earth, *Proc. Phys. Soc.* **43**, 26–45.

CHAPMAN, S. (1931c), The absorption and dissociative or ionizing effect of monochromatic radiation in an atmosphere on a rotating Earth, *Proc. Phys. Soc.* **43**, 483–501.

It was first proposed that the water vapor at the tropopause is saturated and that this cold trap limits the abundance of H_2O at higher altitudes by E. GOLD in 1909 in a report to the British Association in Winnipeg. The concept is developed in

GOLD, E. (1913), The international kite and balloon ascents, *Geophys. Mem.* **1**, No. 5, M.O. 210e (cf. p. 129ff.)

From a series of 16 ascents into the stratosphere between 1943 and 1945 during which humidity measurements were made, BREWER concluded that the low temperature of the tropical tropopause provides the cold trap and that meridional circulation accounts for the low humidity and high ozone content at higher latitudes:

BREWER, A. W. (1949), Evidence for a world circulation provided by the measurements of helium and water vapour distribution in the stratosphere, *Quart. J. Roy. Meteorol. Soc.* **75**, 351–363.

Section 1.6 The Mesopause

The concept of the cold mesopause being strongly influenced by the onset of vibrational relaxation was developed by

CURTIS, A. R. and GOODY, R. M. (1956), Thermal radiation in the upper atmosphere, *Proc. Roy. Soc.* **A 236**, 193–206.

Section 1.7 The Thermosphere

The importance of conduction in maintaining the high temperatures in the thermosphere (which at that time could be only indirectly inferred) was first demonstrated in a classic paper by

SPITZER, L. (1949), The terrestrial atmosphere above 300 km, in "The Atmospheres of the Earth and Planets," (G. P. Kuiper, ed.), pp. 211–247, Univ. Chicago Press, Chicago, [2nd ed., 1952].

Thermospheric theory has since been developed extensively, most notably by

BATES, D. R. (1951), The temperature of the upper atmosphere, *Proc. Phys. Soc.* **B 64**, 805–821.

BATES, D. R. (1959), Some problems concerning the terrestrial atmosphere above about the 100 km level, *Proc. Roy. Soc.* **A 253**, 451–462,

NICOLET, M. (1960), The properties and constitution of the upper atmosphere, *in* "Physics of the Upper Atmosphere," (J. A. Ratcliffe, ed.), pp. 17–71, Academic Press, New York.

The heating of an upper atmosphere by the dissipation of mechanical energy is discussed and compared with radiation sources and sinks by

LEOVY, C. B. (1975), Some energy sources and sinks in the upper atmosphere, *in* "Atmospheres of Earth and the Planets," (B. M. McCormac, ed.), pp. 73–86, D. Reidel Publ. Co., Dordrecht, The Netherlands.

The treatment here of the mesopause condition, defining the mesopause as the height where vibrationally relaxed CO_2 has emitted the entire conductive flux drained from the thermosphere, follows

CHAMBERLAIN, J. W. (1962), Upper atmospheres of the planets, *Astrophys. J.* **136**, 582–593.

Radiation by NO is computed and compared with that by O in

KOCKARTS, G. (1980), Nitric oxide cooling in the terrestrial thermosphere, *Geophys. Res. Lett.* **7**, 137–140.

The derivation of Eq. (1.7.26) follows

HUNTEN, D. M. and DESSLER, A. J. (1977), Soft electrons as a possible heat source for Jupiter's thermosphere, *Planet. Space Sci.* **25**, 817–821.

It is based on a less restricted development by

GROSS, S. H. (1972), On the exospheric temperature of hydrogen-dominated planetary atmospheres, *J. Atmos. Sci.* **29**, 214–218.

Section 1.8.1 Venus

Radio emission from Venus and its interpretation in terms of the temperature and pressure at the planet's surface are discussed by

BARRETT, A. H. and STAELIN, D. H. (1964), Radio observations of Venus and the interpretations. *Space Sci. Rev.* **3**, 109–135,
WOOD, A. T., JR.; WATTSON, R. B.; and POLLACK, J. B. (1968), Venus: Estimates of the surface temperature and pressure from radio and radar measurements, *Science* **162**, 114–116.

Result of the Soviet Venera experiments have been summarized in

AVDUEVSKY, V.; MAROV, M. YA.; and ROZHDESTVENSKY, M. (1970), A tentative model of the atmosphere of planet Venus based on the results of measurements of spaceprobes Venera 5 and Venera 6, *J. Atmos. Sci.* **27**, 561–568.
MAROV, M. YA.; AVDUEVSKY, V.; KERZHANOVICH, V.; ROZHDESTVENSKY, M.; BORODIN, N.; and RYABOV, O. (1973), Venera 8: Measurements of temperature, pressure, and wind velocity on the illuminated side of Venus, *J. Atmos. Sci.* **30**, 1210–1214,
AVDUEVSKY, V.; MAROV, M. YA.; MOSHKIN, B. E.; and RONOMOV, A. E. (1973), Venera 8: Measurements of solar illumination through the atmosphere of Venus, *J. Atmos. Sci.* **30**, 1215–1218.

The Mariner observations of Venus' temperature profile are reported in

FJELDBO, G.; KLIORE, A.; and ESHLEMAN, V. (1971), The neutral atmosphere of Venus as studied with the Mariner 5 radio occultation experiments, *Astron. J.* **76**, 123–140,
HOWARD, H. T., *et al.* (1974), Venus: Mass, gravity field, atmosphere, and ionosphere as measured by the Mariner 10 dual-frequency radio system, *Science* **183**, 1297–1301.

The temperature of the upper atmosphere of Venus is examined theoretically by

DICKINSON, R. E. (1976), Venus mesosphere and thermosphere temperature structure, *Icarus* **27**, 479–493.

Pioneer Venus probe and orbiter results are collected in a special issue of *J. Geophys. Res.* (1980) **85**(A13), 7573–8337.

Figures 1.16 and 1.19 are from

NIEMANN, H. B.; KASPRZAK, W. T.; HEDIN, A. E.; HUNTEN, D. M.; and SPENCER, N. W. (1980), Mass spectrometric measurements of the neutral gas compositon of the thermosphere and exosphere of Venus, *J. Geophys. Res.* **85**, 7817–7827.

Figure 1.17 is from

BRINTON, H. C.; TAYLOR, H. A., Jr.; NIEMANN, H. B.; MAYR, H. G.; NAGY, A. F.; CRAVENS, T. E.; and STROBEL, D. F. (1980), Venus nighttime hydrogen bulge, *Geophys. Res. Lett.* **7**, 865–868.

A monograph incorporating Pioneer Venus and Soviet results is

HUNTEN, D. M.; COLIN, L.; DONAHUE, T. M.; and MOROZ, V. I., eds (1983), "Venus," Univ. Arizona Press, Tucson, Arizona.

Figures 1.14 and 1.15 are from pp. 259 and 354. Figure 1.18 is from

MASSIE, S. T.; HUNTEN, D. M.; and SOWELL, D. R. (1983), Day and night models of the Venus thermosphere, *J. Geophys. Res.* **88**, 3955–3969.

Section 1.8.3 Mars

Infrared radiometer and radio occultation experiments on the Martian surface and atmosphere by Mariner 4 (1965), Mariners 6 and 7 (1969), Mariner 9 (1971–1972), and the Soviet Mars 2 and 3 (1971–1972) have been reviewed in

BARTH, C. A. (1974), The atmosphere of Mars, *Ann. Rev. Earth Planet. Sci.* **2**, 333–367.

The analysis of the low-atmosphere temperatures in terms of heating by dust absorption is due to

GIERASCH, P. J., and GOODY, R. M. (1972), The effect of dust on the temperature of Martian atmosphere, *J. Atmos. Sci.* **29**, 400–402.

Surface temperatures measured by Mariner 9 have been analyzed in

KIEFFER, H. H.; CHASE, S. C.; MINER, E.; MÜNCH, G.; and NEUGEBAUER, G. (1973), Preliminary report on infrared radiometric measurements from the Mariner 9 spacecraft, *J. Geophys. Res.* **78**, 4291–4312.

Viking results are reported in three special issues of *J. Geophys. Res.* (1977), **82**(28), 3951–4684; (1979), **84**(B6), 2793–3007; (1979), **84**(B14), 7909–8519. See, in particular,

HANSON, W. B.; SANATANI, S.; and ZUCCARO, D. R. (1977), The martian ionosphere as observed by the Viking retarding potential analyzers, *J. Geophys. Res.* **82**, 4351–4363.
SEIFF, A., and KIRK, D. B. (1977), Structure of the atmosphere of Mars in summer at mid-latitudes, *J. Geophys. Res.* **82**, 4364–4378.
FJELDBO, G.; SWEETNAM, D.; BRENKLE, J.; CHRISTENSEN, E.; FARLESS, D.; MEHTA, J.; SEIDEL, B.; MICHAEL, W., Jr.; WALLIO, A.; and GROSSI, M. (1977), Viking radio occultation measurements of the Martian atmosphere and topography: Primary mission coverage, *J. Geophys. Res.* **82**, 4317–4324.

Water-vapor results are discussed by

JAKOSKY, B. M., and BARKER, E. S. (1984), Comparison of ground-based and Viking Orbiter measurements of Martian water vapor: variability of the seasonal cycle, *Icarus* **57**, 322–334.

Figure 1.23 is from

HESS, S. L.; RYAN, J. A.; TILLMAN, J. E.; HENRY, R. M.; and LEOVY, C. B. (1980), The annual cycle of pressure on Mars measured by Viking Landers 1 and 2, *Geophys. Res. Lett.* **7**, 197–200.

Section 1.8.5 Mercury and Moon

The Mariner 10 results on Mercury's atmosphere are discussed in

KUMAR, S. (1976). Mercury's atmosphere: A perspective after Mariner 10, *Icarus* **28**, 579–591.
BROADFOOT, A. L. (1976), Ultraviolet spectroscopy of the inner solar system from Mariner 10, *Rev. Geophys. Space Phys.* **14**, 625–627.
BROADFOOT, A. L.; SHEMANSKY, D. E.; and KUMAR, S. (1976), Mariner 10: Mercury's atmosphere, *Geophys. Res. Lett.* **3**, 577–580.

The detection of sodium in the atmosphere of Mercury was reported by

POTTER, A., and MORGAN, T. (1985), Discovery of sodium in the atmosphere of Mercury, *Science* **229**, 651–653.

Potassium was found slightly later:

POTTER, A and MORGAN, T. (1986), Potassium in the atmosphere of Mercury, *Icarus*, **67**, 336–340.

Section 1.9.1 Jupiter

A radiative-transfer analysis for deriving the structure of the troposphere and mesosphere of Jupiter is given in

WALLACE, L.; PRATHER, M.; and BELTON, M. J. S. (1974), The thermal structure of the atmosphere of Jupiter, *Astrophys. J.* **193**, 481–493.

The mesosphere and thermosphere results quoted here are from

STROBEL, D. F., and SMITH, G. R. (1973), On the temperature of the Jovian atmosphere, *J. Atmos. Sci.* **30**, 718–725.

The problems associated with the use of radio occultation experiments to obtain temperature profiles on Jupiter are discussed in

HUBBARD, W. B.; HUNTEN, D. M.; and KLIORE, A. (1975), Effect of the Jovian oblateness on Pioneer 10/11 radio occultations, *Geophys. Res. Lttrs.*, **2**, 265–268,
HUNTEN, D. M. and VEVERKA, J. (1976), Stellar and spacecraft occultations by Jupiter: A critical review of derived temperature profiles, *in* "Jupiter," ed. T. Gehrels, pp. 247–283, Univ Arizona Press, Tucson,
ESHLEMAN, V. R. (1975), Jupiter's atmosphere: Problems and potential of radio occultation, *Science* **189**, 876–878.

A more recent review is

TRAFTON, L. M. (1981), The atmospheres of the outer planets and satellites, *Rev. Geophys. Space Phys.* **19**, 43–89.

Voyager results are reported in a special issue of *J. Geophys. Res.* (1981) **86**(A10), 8121–8844.

Figure 1.26 is from

KUNDE, V.; HANEL, R.; MAGUIRE, W.; GAUTIER, D.; BALUTEAU, J. P.; MARTEN, A.; CHEDIN, A.; HUSSON, N.; and SCOTT, N. (1982), the tropospheric gas composition of Jupiter's north equatorial belt (NH_3, PH_3, CH_3D, GeH_4, H_2O) and the Jovian D/H isotopic ratio, *Astrophys. J.* **263**, 443–467.

The discussion of Jupiter's ionosphere follows

MCCONNELL, J. C.; HOLBERG, J. B.; SMITH, G. R.; SANDEL, B. R.; SHEMANSKY, D. E.; and BROADFOOT, A. L. (1982), A new look at the ionosphere of Jupiter in light of the UVS occultation results, *Planet. Space Sci.* **30**, 151–167.

Section 1.9.2 Saturn, Uranus, and Neptune

A comprehensive monograph, incorporating Voyager results, is

GEHRELS, T., and MATTHEWS, M. S. eds. (1984), "Saturn," Univ. Arizona Press, Tucson, Arizona.

Special issues of journals are

Icarus (1983) **53** (2), 163–387, *J. Geophys. Res.* (1982) **88**(A11), 8625–9018.

Figures 1.28 and 1.29 are from

HANEL, R. A.; CONRATH, B.; FLASAR, F. M.; KUNDE, V.; MAGUIRE, W.; PEARL, J.; PIRRAGLIA, J.; SAMUELSON, R.; HERATH, L.; ALLISON, M.; CRUIKSHANK, D.; GAUTIER, D.; GIERASCH, P.; HORN, L.; KOPPANY, R.; and PONNAMPERUMA, C. (1981), Infrared observations of the Saturnian system from Voyager 1, *Science* **212**, 192–200,
TYLER, G. L.; ESHELMAN, V. R.; ANDERSON, J. D.; LEVY, G. S.; LINDAL, G. F.; WOOD, G. E.; and CROFT, T. A. (1982), Radio science with Voyager 2 at Saturn: Atmosphere and ionosphere and the masses of Mimas, Tethys, and Iapetus, *Science* **315**, 553–558.
SMITH, G. R.; SHEMANSKY, D. E.; HOLBERG, J. B.; BROADFOOT, A. L.; SANDEL, B. R.; and MCCONNELL, J. C. (1983), Saturn's upper atmosphere from the Voyager 2 EUV solar and stellar occultations, *J. Geophys. Res.* **88**, 8667–8678.

An excellent pre-Voyager review for Uranus and Neptune is

BERGSTRALH, J. T., ed. (1984), "Uranus and Neptune," NASA CP-2330.

Figure 1.30 is from the chapter in this volume by

ORTON, G. S. and APPLEBY, J. F. (1984), Temperature structures and infrared-derived properties of the atmospheres of Uranus and Neptune, pp. 89–155.

Voyager Uranus results are in

Science (1986) **233**, 39–109.

Section 1.9.3 Titan

In addition to the references above for Saturn, there is a collection of papers on Titan in *J. Geophys. Res.* (1982) **87**(A3), 1351–1418.

A comprehensive review is

HUNTEN, D. M.; TOMASKO, M. G.; FLASAR, F. M.; SAMUELSON, R. E.; STROBEL, D. F.; and STEVENSON, D. J. (1984), Titan, *in* Gehrels and Matthews, *ibid.*, *pp.* 671–759.

Figure 1.32 is from

SMITH, G. R.; STROBEL, D. F.; BROADFOOT, A. L.; SANDEL, B. R.; SHEMANSKY, D. E.; and HOLBERG, J. B. (1982), Titan's upper atmosphere: Composition and temperature from the EUV solar occultation results, *J. Geophys. Res.* **87**, 1351–1359.

Section 1.9.4 Pluto, Triton, and the Galilean Satellites

Several papers on Pluto appear in *Icarus* (1980) **44**(1), 1-71.

Triton is reviewed by

CRUIKSHANK, D. P. (1984), Physical properties of Neptune's satellites, *in* "Uranus and Neptune," (J. T. Bergstralh, ed.), NASA CP 2330, pp. 425—436.

Many reviews exist for Io, its plasma torus, and their interaction with the Jovian atmosphere. Chapters may be found in

MORRISON, D., ed. (1982), "Satellites of Jupiter," Univ. Arizona Press, Tucson, Arizona.
DESSLER, A. J., ed. (1983), "Physics of the Jovian magnetosphere," Cambridge Univ. Press, Cambridge.
BURNS, J. A., and MORRISON, D., eds. (1985), "Satellites of the Solar System," Univ. Arizona Press, Tucson, Arizona.

PROBLEMS

1.1 *Diffusive equilibrium.* Show that for an atmosphere in diffusive equilibrium the atmospheric scale height is

$$H = \left(\sum_j \frac{N_j/N}{H_j} \right)^{-1}$$

where $H_j = kT/M_j g$.

1.2 *Linear variation of scale height.* Over a region where the temperature changes linearly with height and where $g(r) \approx$ const, show that

$$\frac{p}{p_0} = \left(\frac{H}{H_0}\right)^{-1/\beta} \quad \text{and} \quad \frac{N}{N_0} = \left(\frac{H}{H_0}\right)^{-(1+\beta)/\beta}$$

where $\beta = dH/dr$ and p_0, N_0, and H_0 denote values at a starting distance r_0.

1.3 *Radiative equilibrium.* Assume that solar radiation is absorbed only at the Earth's surface where the albedo is 40%. The re-radiated energy is absorbed mainly by water vapor, which we approximate as a gray absorber with a density scale height of 2 km and a total $\tau_g = 2$. Plot the temperature distribution with height for radiative equilibrium. What is the temperature discontinuity at the ground? What is the gradient in the air temperature near the ground?

1.4 *Chapman Layer.* Show that the maximum absorption in a barometric atmosphere occurs at $\tau_\nu/\mu = 1$ [Eq. (1.5.7)].

1.5 *Chapman stratospheric chemistry.* With the Chapman reactions, what is the daytime rate of change of O_2? Show that this equation adds no new information, beyond what is given by the analogous equations for O and O_3, but merely confirms the conservation of matter.

1.6 *Stratospheric heating.* (a) With the data given below and model atmosphere in Appendix III, find $J_2(z)$ and $J_3(z)$. (b) Use the J's to recompute $[O_3]$ with the "gray u.v." approximation and Chapman chemistry and compare the results for self-consistency with $[O_3]$ in the assumed model. (c) What are the heating rates in degrees per day? What portion arises from O_2 dissociation? (d) Assuming a transparent "gray i.r." atmosphere, compute the temperatures and compare with the model. Show that the κ_ν assumed is consistent with the assumption of optical thinness. Data provided:

$$\begin{aligned}
\alpha_2(O_3) &= 1 \times 10^{-18}\ \text{cm}^2 \quad (1800\text{–}2400\ \text{Å}) \\
\alpha_2(O_2) &= 5 \times 10^{-24}\ \text{cm}^2 \\
\alpha_3(O_3) &= 5 \times 10^{-18}\ \text{cm}^2 \quad (2200\text{–}2900\ \text{Å}) \\
J_2^{(0)} &= 6 \times 10^{-10}\ \text{sec}^{-1} \\
J_3^{(0)} &= 4 \times 10^{-3}\ \text{sec}^{-1} \\
k_{12} &= 6.0 \times 10^{-34}\,(T/300)^{-2.3}\ \text{cm}^6/\text{sec} \\
k_{13} &= 8.0 \times 10^{-12} e^{-2060/T}\ \text{cm}^3/\text{sec} \\
\langle\mu\rangle &= \tfrac{1}{2} \\
\kappa_\nu(\text{i.r.}) &= 1 \times 10^{-3}\ \text{cm}^2/\text{gm}
\end{aligned}$$

1.7 *Thermospheric forbidden oxygen emission.* The triplet ground term, $^3P_{2,1,0}$, of O has the $J = 1$ level at 0.0197 eV and $J = 0$ at 0.0281 eV. The transition probabilities are $A(1,2) = 8.95 \times 10^{-5}\ \text{sec}^{-1}$ and $A(0,1) = 1.70 \times 10^{-5}\ \text{sec}^{-1}$. (a) What is the rate of emission in the two transitions at 200 km? Take $T = 915$°K and $[O] = 4 \times 10^9\ \text{cm}^{-3}$. (b) What is the overhead optical thickness in the centers of each of the two lines? Assume pure Doppler broadening.

1.8 *Mesopause condition.* Compute and make a log plot of the 15μm CO_2 thermal emission rate in the 70–100 km region with the model in Appendix III. Estimate a slope for the curve around 85–90 km and use it to integrate the emission. Find a value of z_0 that satisfies the mesopause condition and compare with the solution (1.7.24).

1.9 *Vibrational relaxation.* Write the equation for statistical equilibrium for the excited vibrational level of the ν_2 fundamental of CO_2 at temperature T. Assume that it is illuminated

from below by black-body radiation at temperature T_0 and allow for induced emission as well as absorption. Show that in the limit of low T_0 the population is given by (1.6.20).

1.10 *Analytic model thermosphere* [after Bates (1959)]. (a) The *geopotential distance* above height z_0 is defined as

$$\zeta = \int_{z_0}^{z} \frac{g(z)}{g(z_0)}\,dz$$

Show that the height may be written as

$$z - z_0 = \frac{\zeta}{1 - \dfrac{\zeta}{r_0 + z_0}}$$

where r_0 is the radius of the planet. (b) Let the temperature be represented by the formula

$$T(z) = T(\infty)[1 - a\exp(-\tau\zeta)]$$

where a and τ are specified constants:

$$a \equiv 1 - \frac{T(z_0)}{T(\infty)}$$

$$\tau \equiv \frac{(dT/dz)_0}{T(\infty) - T(z_0)}$$

Show by integrating (1.1.5) that the number density of a constituent in diffusive equilibrium is

$$N(z) = N(z_0)\left(\frac{1-a}{\exp(\tau\zeta) - a}\right)^{1+\gamma} \exp(\tau\zeta)$$

where

$$\gamma = \frac{1-a}{\tau H_0}$$

and H_0 is the pressure scale height of the constituent at z_0. (c) Take $T(\infty) = 1000$°K and at $z_0 = 120$ km take the O density as $N_0 = 9.3 \times 10^{10}\ \text{cm}^{-3}$, $T(z_0) = 360$°K and $(dT/dz)_{z_0} = 12$°K/km. Compute the temperature and O density at $\zeta = 79$ and 359 km and compare with the model in Appendix III.

1.11 *Thermospheric temperature profile.* (a) Complete the derivation of Eq. (1.7.26). Indicate how the differential equation, including sources and sinks, could be set up for a numerical finite-difference solution. (b) Using the heat flux from Eq. (1.7.22) and the conductivity for O from Table 1.2, estimate the thermospause temperature for the Earth. (To ascertain the optical depth use a cross section of $10^{-17}\ \text{cm}^2$ and work out the column density from the data in the Appendices.) Repeat with twice the heat flux and compare with the actual Earth at solar minimum and maximum. (c) Mars and Venus both have CO_2 atmospheres and, therefore, differ in Eq. (1.7.26) only in Q and g. Would you expect similar thermopause temperatures? Why does gravity play this kind of role?

1.12 *Venus thermopause temperature.* Proceed as in Problem 1.11, but include a heating efficiency of 0.1 and other parameters adjusted to Venus (solar flux; CO_2 atmosphere; $T_0 = 180$°K; $\tau_0/\langle\mu\rangle = 250$).

1.13 *Jupiter thermopause temperature.* Evaluate Eq. (1.7.26) for Jupiter with the following data: heating efficiency, 0.82; mesopause temperature, 150°K, and mesopause density, 5×10^{13} cm^{-3}.

1.14 *Titan mesosphere mean temperature.* Voyager observations give (p,T) equal to (1.0 mbar, 167°K) at 190 km, and (6.2×10^{-9} mbar, 165°K) at 1265 km. With the hydrostatic equation and a mean mass of 28 amu, find the mean temperature of the region between. Do not forget the variation of gravity with height (cf. Problem 1.10).

Chapter 2
HYDRODYNAMICS OF ATMOSPHERES

2.1 Basic Equations

2.1.1 Equations in an Inertial Frame

The basic equations relating mass density ρ, pressure p, temperature T, and the three velocity components of $\mathbf{v}$ (u, v, w) are the equations of continuity, motion, state, and energy conservation. The continuity equation expresses the conservation of mass,

$$\frac{\partial \rho}{\partial t} = -\nabla \cdot (\rho \mathbf{v}) \tag{2.1.1}$$

which states that the local rate of increase in mass density is equivalent to the fluid's "convergence." Alternatively, it is common to write continuity in terms of the *substantial derivative*, taken along the path followed by an element of fluid. Thus

$$\frac{d\rho}{dt} \equiv \frac{\partial \rho}{\partial t} + \mathbf{v} \cdot \nabla \rho = -\nabla \cdot (\rho \mathbf{v}) + \mathbf{v} \cdot \nabla \rho \tag{2.1.2}$$

Expanding the divergence we have

$$\frac{d\rho}{dt} = -\rho \nabla \cdot \mathbf{v} \tag{2.1.3}$$

In the special case of an incompressible fluid,

$$\nabla \cdot \mathbf{v} = 0 \tag{2.1.4}$$